The Astrophysical Journal, 950:141 (17pp), 2023 June 20 https://doi.org/10.3847/1538-4357/acd187

The ELM Survey South. II. Two Dozen New Low-mass White Dwarf Binaries

Alekzander Kosakowski[1], Warren R. Brown[2], Mukremin Kilic[3], Thomas Kupfer[1], Antoine Bédard[4], A. Gianninas[5], Marcel A. Agüeros[6,7], and Manuel Barrientos[3]
[1] Department of Physics and Astronomy Texas Tech University 2500 Broadway Lubbock, TX 79409, USA; a.kosakowski@protonmail.com
[2] Center for Astrophysics, Smithsonian Astrophysical Observatory 60 Garden St., Cambridge, MA 012138 USA
[3] Homer L. Dodge Department of Physics and Astronomy University of Oklahoma 1667 K Street NW, Suite 800 Norman, OK 73072, USA
[4] Department of Physics, University of Warwick, Gibbet Hill Road, Coventry CV4 7AL, UK
[5] Physics Department, Trinity College 330 Summit Street, Hartford, CT 06106, USA
[6] Department of Astronomy, Columbia University, 550 West 120th Street, New York, NY 10027, USA
[7] Laboratoire d'astrophysique de Bordeaux, Univ. Bordeaux, CNRS, B18N, Allée Geoffroy Saint-Hilaire, F-33615 Pessac, France
Received 2023 March 10; revised 2023 April 21; accepted 2023 April 25; published 2023 June 19

Abstract

We present the results from our ongoing spectroscopic survey targeting low-mass white dwarf binaries, focusing on the southern sky. We used a Gaia DR2- and eDR3-based selection and identified 28 new binaries, including 19 new extremely low-mass (ELM) white dwarfs, one short period, likely eclipsing, DABZ, and two potential LISA binaries. We present the orbital and atmospheric parameters for each new binary based on our spectroscopic follow up. Four of our new binaries show periodic photometric variability in TESS 2 minutes cadence data, including one new eclipsing double-lined spectroscopic binary. Three others show periodic photometric variability in ZTF, including one new eclipsing binary. We provide estimates for the inclinations and scaled component radii for these ZTF variables, based on light-curve modeling of our high-speed photometric follow-up observations. Our observations have increased the sample of ELM Survey binaries identified in the southern sky to 41, an increase of 64%. Future time domain surveys, such as BlackGEM and the Vera C. Rubin Observatory Legacy Survey of Space and Time, will efficiently identify photometric variables in the southern sky and significantly increase the population of southern sky low-mass white dwarf binaries, leading to a more complete all-sky population of these systems.

Unified Astronomy Thesaurus concepts: Compact binary stars (283); Eclipsing binary stars (444); White dwarf stars (1799); Spectroscopy (1558)

Supporting material: machine-readable tables

1. Introduction

Extremely low-mass (ELM; $M \lesssim 0.3\,M_{\odot}$) white dwarfs are a relatively rare class of He-core white dwarfs which form after early severe mass loss. Because the main-sequence lifetime of low-mass stars can exceed a Hubble time, the ELM white dwarfs observed today are not expected to have formed through single-star evolution. With the exception of the extreme mass loss of high-metallicity stars (see Kilic et al. 2007), ELM white dwarfs are expected to form through binary evolution, including one or more episodes of common envelope evolution (Li et al. 2019). The result of this binary evolution is a population of evolved compact binaries containing low-mass He-core white dwarfs with evolved companions.

These low-mass white dwarf binaries are important for studying both binary evolution and the formation rates of various exotic systems. Shen (2015) and Brown et al. (2016b) show that most white dwarf binaries may merge and form other exotic systems such as extreme helium stars (Zhang et al. 2014), accreting AM CVn binaries (Kilic et al. 2016), or massive single white dwarfs (Kilic et al. 2023). Binaries with well-constrained physical parameters have also been used to place constraints on the efficiency of common envelope ejection (see Scherbak & Fuller 2023).

The ELM Survey (Brown et al. 2010; Kilic et al. 2011; Brown et al. 2012; Kilic et al. 2012; Brown et al. 2013; Gianninas et al. 2015; Brown et al. 2016a, 2020, 2022) is a spectroscopic survey targeting these low-mass white dwarf binaries based on photometry from sky surveys, such as the Sloan Digital Sky Survey (SDSS; Abazajian et al. 2003) and Pan-STARRs (Chambers et al. 2016). Kosakowski et al. (2020) expanded the ELM Survey into the southern sky using photometry from SkyMapper (Onken et al. 2019) and VST ATLAS (Shanks et al. 2015), and found that a Gaia-based selection is efficient for identifying ELM white dwarf binaries. In total, previous ELM Survey studies have constrained the orbits and atmospheric parameters of 120 unique low-mass white dwarf binaries (Brown et al. 2020; Kosakowski et al. 2020; Brown et al. 2022). Similar studies have created catalogs of ELM white dwarf candidates using Gaia DR2 astrometry (see Pelisoli & Vos 2019) and single-epoch spectroscopy from LAMOST DR8 (see Wang et al. 2022), many of which still require follow-up observations to confirm their nature.

In this work, we continue the ELM Survey South with our search for low-mass white dwarf binaries in the southern sky using Gaia DR2 and eDR3. While we focused on objects in the southern sky, our Gaia-based selection included many northern sky objects, which we include in this work.

2. Target Selection

Our target selection made use of parallax and color measurements from Gaia DR2 (Gaia Collaboration et al. 2018) and eDR3

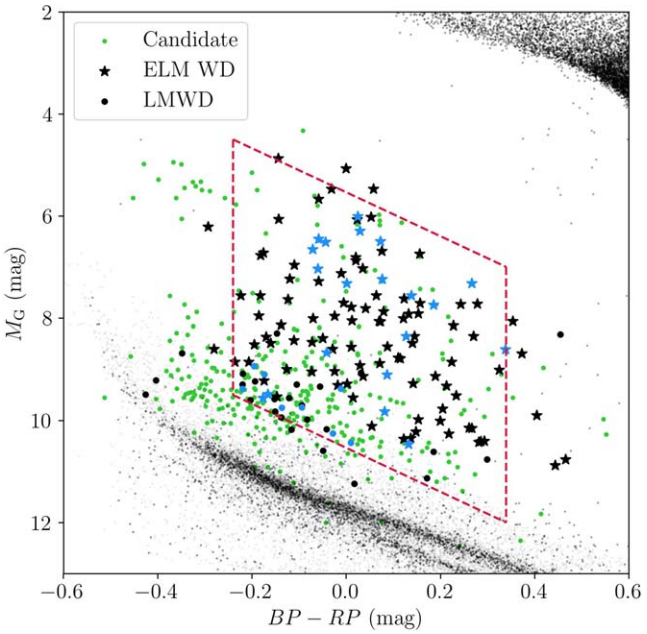

Figure 1. Gaia color–magnitude diagram showing the target selection box described in the text. The 28 new binaries identified in this work are represented with blue symbols, while the previous ELM Survey binaries are represented as black symbols. Stars represent ELM white dwarfs ($M \lesssim 0.3\ M_\odot$). Filled circles represent low-mass white dwarfs. Green circles represent our observed candidates selected through our Gaia DR2 and eDR3 selection.

(Gaia Collaboration et al. 2021, 2022) based on previous ELM Survey discoveries. Figure 1 displays the locations of our observed objects in a Gaia DR3 color–magnitude diagram. The 28 new binaries from this work are plotted with blue symbols while previous ELM Survey binaries are plotted as black symbols. Green points represent other objects observed as part of this work with PARALLAX_OVER_ERROR > 3, PARALLAX > 0.5, and no cuts to RUWE, for which we have obtained at least one optical spectrum. We draw a box around the region surrounding the main concentration of ELM Survey ELM white dwarf binaries, defined by

$$-0.24 < (\mathrm{BP} - \mathrm{RP}) < 0.34,$$
$$M_G > 4.31(\mathrm{BP} - \mathrm{RP}) + 5.53,$$
$$M_G < 4.31(\mathrm{BP} - \mathrm{RP}) + 10.53.$$

Within this box, we have observed 217 objects, including the 28 new low-mass white dwarf binaries presented in this work. Among our observed objects, we identify 27 additional ELM white dwarf candidates based on model atmosphere fits to our follow-up spectroscopy, including 17 which fall within the parameter space of the "clean" sample of ELM white dwarfs of Brown et al. (2020). Our ongoing follow up finds that at least half of these spectroscopic candidates show significant radial velocity variability, but have unconstrained orbital parameters. These additional binaries will be presented in a future publication. Most of our observed sample contains single white dwarfs with $\log g \approx 7.5$.

3. Observations

We used a similar observing strategy as in previous ELM Survey publications: we obtained one optical spectrum for each of our candidates to confirm their nature and perform spectroscopic fitting with model atmospheres. For objects consistent with ELM white dwarfs ($5.0 \lesssim \log g \lesssim 7.2$), we obtained multiple additional spectra to check for radial velocity variability and constrain their orbital periods. Candidates which do not show significant radial velocity variability, or which show atmospheric parameters inconsistent with ELM white dwarfs, are excluded from the extensive follow up.

Our observing strategy favors identifying short-period binaries ($P \lesssim 6$ hr) with large velocity semiamplitudes, which form through common envelope interaction. Binaries with longer orbital periods and lower velocity semiamplitudes, which likely form through stable Roche Lobe overflow, are less likely to be detected and constrained through our observing strategy, while those that are identified require more resources to constrain through radial velocity follow up.

In this section we briefly describe the resources used for our follow-up observations, including the telescopes, instruments, and configurations.

3.1. Southern Astrophysical Research Telescope

We used the Southern Astrophysical Research Telescope (SOAR) 4.1 m telescope with the Goodman spectrograph (Clemens et al. 2004) configured with the 930 lines mm^{-1} grating and 1.″01 slit, resulting in a spectral resolution ≈2.6 Å over the wavelength range 3550–5300 Å. These data were taken as part of the NOAO programs 2019B-0004, 2020B-0013, and 2021A-0007, and NOIRLab 2022A-161017.

3.2. Gemini South and North

We used the Gemini South 8.1 m telescope, located on Cerro Pachón in Chilé with the GMOS-S spectrograph and the Gemini North 8.1 m telescope, located on Mauna Kea in Hawai'i with the GMOS spectrograph, configured with the 0.″5 and 1.″0 slits and the B600 grating (600 lines mm^{-1}) in first-order centered on $\lambda_{\mathrm{center}} = 5150$ Å. These configurations resulted in resolutions ≈2.8 Å and ≈5.5 Å over the spectral range 3600–6750 Å. These data were obtained as part of the programs GN-2021A-Q-203, GN-2021A-Q-300, GS-2020B-Q-304, GS-2021A-Q-300, and GS-2021B-Q-304.

3.3. Walter Baade Magellan Telescope

We used the 6.5 m Walter Baade Magellan 1 Telescope at the Las Campanas Observatory in Chilé with the Magellan Echellette (MagE) spectrograph and the 0.″85 slit, resulting in a resolving power $R \approx 4800$ covering the wavelength range 3600–7000 Å.

3.4. Fred Lawrence Whipple Observatory

We used the 1.5 m Tillinghast telescope at Fred Lawrence Whipple Observatory (FLWO) located on Mt. Hopkins in Arizona. Our primary setup used the FAST spectrograph with the 1.″5 slit and 300 lines mm^{-1} grating, resulting in a spectral resolution ≈3.6 Å covering the spectral range 3500–7400 Å. A handful of observations used a slightly different setup with the 1.5 Å slit and 600 lines mm^{-1} grating, resulting in a spectral resolution ≈1.8 Å covering the spectral range 3650–5300 Å.

3.5. MMT Observatory

We used the 6.5 m MMT with the blue channel spectrograph, primarily with the 1.″25 slit and 832 lines mm^{-1} grating, resulting in ≈1.2 Å resolution over the wavelength range

3600–4500 Å. However, a handful of our observations used the 1.″0 slit with the 832 lines mm^{-1} grating, resulting in a spectral resolution ≈1.0 Å over roughly same wavelength range.

3.6. MDM Observatory

We used the 2.4 m Hiltner telescope at the MDM observatory, located in Kitt Peak, Arizona, with the OSMOS spectrograph, the 1.″2 slit, and the blue grism ($R \sim 1600$), resulting in a spectral resolution of 3.6 Å over the wavelength range 3600–5930 Å.

3.7. McDonald Observatory

We used the 2.1 m Otto Struve telescope at the McDonald Observatory near Fort Davis, Texas to obtain high-speed photometric follow up of our binaries to confirm the variability seen in various sky survey data archives. We used the ProEM frame-transfer CCD detector with either the BG40, *g*-, *r*-, or *i*-band filters.

4. Spectroscopic Analysis

4.1. Data Reduction and Calibration

Data reduction was performed using standard IRAF procedures, including bias correction, flat-fielding, aperture extraction, wavelength calibration, and flux calibration with spectrophotometric standard star observations obtained on the same night as each science exposure.

To ensure an accurate wavelength solution for each spectrum, we paired each science exposure with a calibration lamp spectrum taken within ≈15 minutes at the same telescope position as the corresponding science exposure, resulting in a wavelength calibration accuracy of 2–3 $km\,s^{-1}$, as tested against night sky lines.

4.2. Radial Velocities

We measured the radial velocities of each of our spectra using a cross-correlation method with the IRAF package XCSAO (Kurtz & Mink 1998). Each spectrum was cross-correlated with a low-mass white dwarf template spectrum and corrected to zero velocity. We combined the individual zero-velocity object-specific spectra to create a single high-quality, zero-velocity spectrum for each object which we use for atmospheric modeling. Finally, we cross-correlated the combined zero-velocity template spectrum for each object with their single-exposure component spectra to obtain our final radial velocity measurements. Our radial velocity measurements for each binary are presented in Table A1. We fit a circular orbit to our radial velocity measurements using a Monte Carlo approach based on Kenyon & Garcia (1986) to estimate the orbital period P, velocity semiamplitude K, and systemic velocity γ.

4.3. Atmospheric Parameters

We estimated the atmospheric parameters $T_{\rm eff}$ and $\log g$ for the primary star in each of our binaries through fitting a grid of 1D pure-hydrogen atmosphere models to our high signal-to-noise ratio (S/N), combined, zero-velocity spectra. The details of this process are described in Gianninas et al. (2011, 2014, 2015). In short, we applied a Levenberg–Marquardt minimization algorithm to fit the normalized Balmer line profiles of Hβ through H12, where visible, to a grid of pure-hydrogen model atmospheres convolved to the spectral resolution of the observed spectra, defined by the observation instrument setup. Our parameter estimates are reliable for binaries in which the companion does not contribute a significant amount to the total system light.

Cool objects, with temperatures $T_{\rm eff} \lesssim 10{,}000$ K, return systematically large $\log g$ when fit with 1D stellar models (see Tremblay et al. 2011). Thus, we apply a 3D correction to the fits of cool objects using the equations provided in Tremblay et al. (2015).

Our minimization process returns internal uncertainties which are most sensitive to the flux calibration and S/N of the input spectrum. We add in quadrature the external uncertainties of $\sigma_{T_{\rm eff}} = 1.4\%$ and $\sigma_{\log g} = 0.042$ dex, as presented in Liebert et al. (2005), to each of our reported values.

Table A2 presents the atmospheric parameters for our observed sample (Figure 1, green points) with $\log g > 5.0$. A representative optical spectrum for many of these objects is available in an online Zenodo archive: doi:10.5281/zenodo.7849976 (Kosakowski et al. 2023) in FITS format.

5. Archival Light-curve Data

Large-scale time domain surveys are a valuable resource for efficiently identifying transients and periodic variables. While these time domain surveys do not replace conventional target selection methods, when paired with color surveys and the precise astrometry from Gaia, it is possible to perform follow-up observations efficiently for characterizing photometrically variable sources.

We made use of the publicly available online data archives of the Transiting Exoplanet Survey Satellite (TESS; Ricker et al. 2015) and the Zwicky Transient Facility (ZTF; Bellm et al. 2019; Graham et al. 2019; Masci et al. 2019) DR10 to confirm the photometric variability of our targets and constrain their orbital periods.

We used the computational resources of the Texas Tech University High Performance Computing Center to perform searches for periodic variability in each of our target light curves from both the TESS and ZTF public data archives. We used two algorithms to identify different types of photometric variability.

For sinusoidal variability, typically caused by a tidally distorted star in a compact binary, relativistic beaming, strong reflection effects, stellar rotation, or low-amplitude pulsations, we used the ASTROPY (Astropy Collaboration et al. 2013, 2018, 2022) implementation of the Lomb–Scargle (LS) periodogram (Lomb 1976; Scargle 1982; VanderPlas 2018), searching periods between 5 minutes and 684 minutes.

To identify eclipsing binaries, we make use of a generic Box Least Squares (BLS; Kovács et al. 2002) algorithm, which attempts to fit box-shaped eclipses to light-curve data phase-folded at periods within the provided frequency grid. Specifically, our BLS algorithm searched for eclipse durations between 0.1% and 10.0% of the orbit and orbital periods between 5 minutes and 684 minutes. The BLS algorithm is ideal for identifying eclipsing systems with sharp ingress and egress features, such as eclipsing binaries containing white dwarfs.

5.1. TESS High-cadence Data Archive

TESS is a space-based all-sky survey satellite designed to identify exoplanets through transit detections in 27 days long

pointings, covering a 24×96 deg^2 field of view in a broadband filter (≈6000–10,000 Å). The original mission (2018–2020) obtained 30 minutes cadence data in Full Frame Images (FFIs) with select fields obtaining 2 minutes high-cadence observations. The recent extended mission (2020–2022) has improved these to 10 minutes cadence FFIs and 20 s high-cadence fields. While the plate scale for TESS is large ($\approx 21'' \, \mathrm{px}^{-1}$), objects that show photometric variability in TESS data are typically very well sampled.

We searched the Barbara A. Mikulski Archive for Space Telescopes (MAST), through the Python module ASTROQUERY.MAST[8], to identify the TESS Input Catalog (TIC; Stassun et al. 2018) target ID for each of our objects. Using the TIC IDs, we downloaded the TESS 2 minutes and 20 s cadence light-curve data through the online TESS archive[9].

For each sector of TESS data we recovered, we removed lower-quality data, based on the bit flags described on the TESS Data Quality Overview webpage[10], following the steps outlined in the Jupyter Notebook examples provided through the Space Telescope Science Institute's GitHub page[11]. We combined data across multiple sectors by simply dividing each sector's light curve by its median PDCSAP flux value (aperture photometry corrected for common instrumental systematics and trends) and appending each scaled sector light curve together.

5.2. ZTF Data Archive

ZTF is an optical time domain survey designed to image the entire northern sky down to ≈20.5 mag every two days in two filters, ZTF-g and ZTF-r, with ZTF-i sampled less frequently. The ZTF survey uses the 48-inch Schmidt Telescope at the Palomar Observatory in California with a 48 deg^2 field of view.

We performed a cone-search on the public Data Release[12] 10 (DR10) data archive using a 5″ search radius centered on the Gaia DR2 or eDR3 coordinates for each of our objects. Because ZTF assigns different object IDs for the same object in different filters, we combined data for object detections within 2.″5 of each coordinate pair returned within our 5″ search radius. This process separates nearby ($2.''5 < d < 5.''0$) objects in relatively crowded fields.

To increase the temporal sampling of the ZTF light curves, we artificially shifted the r-band and i-band data such that their median magnitudes matched the median value of the g-band data. We then used this median-combined light curve in our periodicity search.

Many of our objects which show short-period photometric variability in ZTF were included in the ZTF deep-drilling survey, which targets specific fields for continuous observations over ≈90 minutes in the ZTF-r band (Kupfer et al. 2021). These deep-drilling fields provide significant orbital phase coverage that would otherwise be relatively sparse in the standard ZTF northern sky survey.

[8] https://astroquery.readthedocs.io/en/latest/mast/mast.html
[9] https://archive.stsci.edu/tess/bulk_downloads/bulk_downloads_ffi-tp-lc-dv.html
[10] https://outerspace.stsci.edu/display/TESS/2.0+-+Data+Product+Overview
[11] https://github.com/spacetelescope/notebooks/
[12] https://www.ztf.caltech.edu/ztf-public-releases.html

6. Results

We have constrained the atmospheric parameters and orbital periods for 28 new binaries identified through our target selections. In this section, we present the details for the eight binaries which require additional explanation, such as those with additional constraints from light-curve data or those with unusual spectra. The remaining objects are summarized in Table 1. We display the $\log g$–$T_{\rm eff}$ distribution for each of these objects in Figure 2.

6.1. J0215+0155

We obtained 112 radial velocity measurements for J021506.244+015503.363 (J0215+0155; GAIA DR3 2515358251735261696), resulting in best-fitting orbital parameters of $P_{\rm RV} = 9.3106$ hr, $K = 186.4 \pm 1.5$ km s^{-1}, and $\gamma = -49.4 \pm 1.1$ km s^{-1}. Together with Gaia DR3 astrometry, we estimated the Galactic space velocities $[U, V, W] = [121 \pm 1, -37 \pm 1, -59 \pm 1]$ km s^{-1}, (U positive toward the Galactic center), corrected for the motion of the local standard of rest (Schönrich et al. 2010).

We determine Galactic disk and halo membership by computing the Mahalanobis distance between the measured Galactic space velocities and the velocity distributions for thick disk and halo populations using the average velocities and velocity dispersions from Chiba & Beers (2000). Specifically, we compared against the velocity distributions defined by $[\langle U\rangle, \langle V\rangle, \langle W\rangle]_{\rm Disk} = [4 \pm 46, -20 \pm 50, -3 \pm 35]$ km s^{-1} and $[\langle U\rangle, \langle V\rangle, \langle W\rangle]_{\rm Halo} = [17 \pm 141, -187 \pm 106, -5 \pm 94]$ km s^{-1} for the thick disk and halo, respectively. Our measurements for J0215+0155 are consistent with Galactic halo membership.

Our pure-hydrogen model atmosphere fits to the summed zero-velocity spectrum of J0215+0155 result in best-fitting atmospheric parameters of $T_{\rm eff} = 11{,}310 \pm 180$ K and $\log g = 5.34 \pm 0.05$, corresponding to a white dwarf with mass $M_1 = 0.29 \pm 0.02 \, M_\odot$ based on the halo-metallicity models for He-core white dwarfs from Istrate et al. (2016). With the velocity semiamplitude known and orbital period known, we used the binary mass function

$$\frac{(M_2 \sin i)^3}{(M_1 + M_2)^2} = \frac{PK^3}{2\pi G}, \quad (1)$$

to estimate the minimum companion mass $M_{2,\rm min} = 0.59 \pm 0.02 \, M_\odot$.

We find three sectors of TESS 2 minutes cadence data for J0215+0155 (TIC 270432557). Our LS algorithm identifies weak (∼1% level) periodic variability at $f_{\rm TESS} = 5.1556$ cycles day^{-1}, equal to half of the orbital period determined through the radial velocity measurements. Figure 3 (upper left) displays the phase-folded TESS light curve of J0215+0155 and its LS power spectrum. A smaller peak can be seen in the power spectrum at the true orbital frequency of the system. The dominant frequency at 5.1556 cycles day^{-1} is likely caused by tidal distortions in the compact binary. A detailed high-precision, follow-up, light-curve analysis may help place constraints on the orbital inclination and mass ratio of this binary (see, for example, Hermes et al. 2014).

6.2. J0221+1710

We obtained 19 radial velocity measurements of J022110.832 +171049.182 (J0221+1710; GAIA DR3 79808158877017216),

Table 1
White Dwarf Parameters Determined Through Optical Spectroscopy for the 28 New Binaries Identified in This Work

Object Name	R.A. (2016.0)	Decl. (2016.0)	$T_{\rm eff}$ (K)	$\log g$ (cm s^{-2})	M_1 ($M_\odot$)	Gaia G (mag)	Gaia Parallax (mas)
J0135+2359	01:35:00.856	+23:59:46.091	14,130 ± 210	6.46 ± 0.05	0.21 ± 0.04	18.7	1.18 ± 0.29
J0155−4148	01:55:34.866	−41:48:18.433	11,250 ± 170	5.75 ± 0.05	0.22 ± 0.02	15.7	2.08 ± 0.03
J0215+0155[c]	02:15:06.244	+01:55:03.363	11,310 ± 180	5.34 ± 0.05	0.29 ± 0.02	14.3	2.15 ± 0.03
J0221+1710[c]	02:21:10.832	+17:10:49.182	13,400 ± 200	7.01 ± 0.04	0.27 ± 0.01	17.7	3.58 ± 0.12
J0256+4405	02:56:35.153	+44:05:27.363	18,170 ± 350	5.56 ± 0.06	0.22 ± 0.02	15.8	1.40 ± 0.04
J0450−0145[c]	04:50:13.108	−01:45:48.150	9560 ± 140	5.58 ± 0.06	0.19 ± 0.02	17.7	0.91 ± 0.11
J0501−2312[c]	05:01:29.865	−23:12:04.397	21,440 ± 330	7.21 ± 0.05	0.36 ± 0.01	18.0	1.64 ± 0.10
J0517−1153[c]	05:17:24.974	−11:53:25.849	16,650 ± 300	5.96 ± 0.06	0.19 ± 0.02	16.2	1.47 ± 0.04
J0545−1902	05:45:45.301	−19:02:45.499	22,850 ± 340	7.34 ± 0.05	0.40 ± 0.02	17.3	2.59 ± 0.07
J0725−1245	07:25:27.362	−12:45:46.824	21,920 ± 420	7.42 ± 0.06	0.42 ± 0.02	18.9	1.51 ± 0.25
J1121+6052[a]	11:21:57.163	+60:52:10.265	11,690 ± 170	5.41 ± 0.05	0.19 ± 0.01	16.0	1.33 ± 0.04
J1129+4715[c]	11:29:14.162	+47:15:01.726	11,610 ± 170	5.32 ± 0.05	0.19 ± 0.01	16.1	1.18 ± 0.04
J1240−0958	12:40:32.501	−09:58:59.603	14,020 ± 280	5.24 ± 0.06	0.20 ± 0.02	19.0	1.30 ± 0.30
J1255−1853	12:55:39.147	−18:53:32.101	11,270 ± 200	5.25 ± 0.06	0.19 ± 0.01	17.8	0.55 ± 0.13
J1459−1920	14:59:02.159	−19:20:33.552	8740 ± 130	5.66 ± 0.07	0.26 ± 0.02	18.1	0.71 ± 0.16
J1506−1125	15:06:12.345	−11:25:11.994	(22,050 ± 320)	(7.44 ± 0.05)	(0.43 ± 0.02)	17.0	2.42 ± 0.10
J1526−2711[c]	15:26:01.115	−27:11:56.660	17,460 ± 260	7.31 ± 0.05	0.37 ± 0.02	18.3	1.61 ± 0.18
J1553+6736[c]	15:53:28.008	+67:36:10.560	9610 ± 150	6.11 ± 0.11	0.22 ± 0.04	16.5	2.36 ± 0.04
J1555+1007[c]	15:55:15.894	+10:07:24.851	13,340 ± 220	7.32 ± 0.05	0.35 ± 0.02	18.2	2.52 ± 0.15
J1657−0417	16:57:24.888	−04:17:22.348	17,750 ± 270	6.85 ± 0.05	0.27 ± 0.02	18.3	2.04 ± 0.18
J1808+2723	18:08:38.994	+27:23:12.216	10,630 ± 270	6.35 ± 0.29	0.22 ± 0.04	15.5	2.82 ± 0.03
J1812+0525[b]	18:12:38.471	+05:25:29.868	8960 ± 130	5.96 ± 0.08	0.28 ± 0.03	18.9	0.85 ± 0.26
J1832+2031[c]	18:32:36.539	+20:31:08.202	19,080 ± 290	6.74 ± 0.05	0.29 ± 0.03	17.6	1.61 ± 0.08
J2013−1310[c]	20:13:53.498	−13:10:41.750	11,200 ± 190	7.42 ± 0.06	0.37 ± 0.02	18.7	2.21 ± 0.25
J2049+3351[b]	20:49:51.274	+33:51:53.126	17,500 ± 500	5.85 ± 0.05	…	18.7	0.51 ± 0.16
J2102−4145a[a]	21:02:20.456	−41:45:01.736	12,700 ± 500	7.20 ± 0.05	0.32 ± 0.01	15.8	6.07 ± 0.04
J2102−4145b[a]	21:02:20.456	−41:45:01.736	13,400 ± 500	7.45 ± 0.05	0.39 ± 0.01	…	6.07 ± 0.04
J2243−4511	22:43:27.479	−45:11:18.404	15,880 ± 230	7.04 ± 0.05	0.29 ± 0.01	17.4	2.57 ± 0.09
J2303−2614[a,c]	23:03:23.542	−26:14:59.917	11,280 ± 160	5.43 ± 0.05	0.18 ± 0.01	13.8	3.12 ± 0.02

Notes. Our reported atmospheric parameters $T_{\rm eff}$ and $\log g$ include the external uncertainties of $\sigma_{T_{\rm eff}} = 1.4\%$ and $\sigma_{\log g} = 0.042$ dex from Liebert et al. (2005). Binaries which show photometric variability in the TESS 2 minute cadence or ZTF data archives are marked. We apply 3D corrections using the equations from Tremblay et al. (2015) for objects cooler than $T_{\rm eff} \approx 10{,}000$ K. The atmospheric parameter values for J1506−1125 displayed in this table are based on single-star models. We describe our multicomponent modeling to J1506−1125 in Section 6, which does not identify a unique solution.

[a] Photometric variability: TESS high cadence.

[b] Photometric variability: ZTF.

[c] Pelisoli & Vos (2019) ELM white dwarf candidate.

(This table is available in machine-readable form.)

resulting in the orbital parameters $P_{\rm RV} = 1.4709 \pm 0.0005$ hr, $K = 347.9 \pm 4.2$ km s^{-1}, and $\gamma = 35.3 \pm 3.7$ km s^{-1}. With precise Gaia astrometry, we estimated Galactic space velocities [U, V, W] = [−40.4 ± 1.8, −4.8 ± 1.6, 7.5 ± 1.7] km s^{-1}, which are well within the 2σ velocity ellipsoid for the Galactic disk.

Our best-fitting pure-hydrogen atmospheric parameters to J0221+1710 are $T_{\rm eff} = 13{,}400 \pm 200$ K and $\log g = 7.01 \pm 0.04$, corresponding to a white dwarf with mass $M_1 = 0.27 \pm 0.01\,M_\odot$, based on the Z = 0.02 model tracks of Istrate et al. (2016).

Our BLS periodicity search on the ZTF DR13 data archive identified periodic $\Delta m \approx 0.2$ mag eclipses at $P_{\rm ZTF,BLS} = 88.2508$ minutes (1.4708 hr), in agreement with our orbital period obtained through radial velocity measurements.

We obtained high-speed g- and r-band photometry using the McDonald 2.1 m telescope on UT 2022 October 01 and 02. Our observations cover three eclipses in each filter. We used EXPTIME = 10 s, resulting in five mideclipse data points and four data points during the ingress or egress per eclipse for the ≈90 s eclipse duration.

We modeled the geometry of the binary by simultaneously fitting the g- and r-band light curves using LCURVE (Copperwheat et al. 2010), fitting for the component radii ($r_i = \frac{R_i}{a}$) and the temperature of the companion ($T_{\rm eff,2}$). We fixed the orbital period to the value obtained from our ZTF BLS analysis and used the results from our spectroscopic follow up ($T_{\rm eff,1}$, $\log g_1$, and K_1) as Gaussian priors to our light-curve modeling. We interpolated over the grid of gravity darkening and quadratic limb-darkening coefficients from Claret et al. (2020) for our primary star based on our spectroscopic values and used values for a companion with $T_{\rm eff,2} = 10{,}000$ K and $\log g_2 = 8.0$.

The most-probable system parameters from our light-curve fitting are $R_1 = 0.028 \pm 0.001\,R_\odot$, $R_2 = 0.012 \pm 0.001\,R_\odot$, $i = 89\overset{\circ}{.}0 \pm 0\overset{\circ}{.}2$, and $T_{\rm eff,2} = 5200^{+400}_{-500}$ K. However, given the quality of our McDonald r-band light-curve data during the eclipse, we adopt the 3σ upper limit to the temperature of the companion. Our most-probable model parameters are summarized in Table 3. Figure 4 displays our phase-folded McDonald 2.1 m g- (top) and r-band (bottom) light curves with the best-fitting model overplotted in red.

With the inclination and radial velocity semiamplitude known, we used the binary mass function to calculate the companion mass, $M_2 = 0.58 \pm 0.02\,M_\odot$, corresponding to

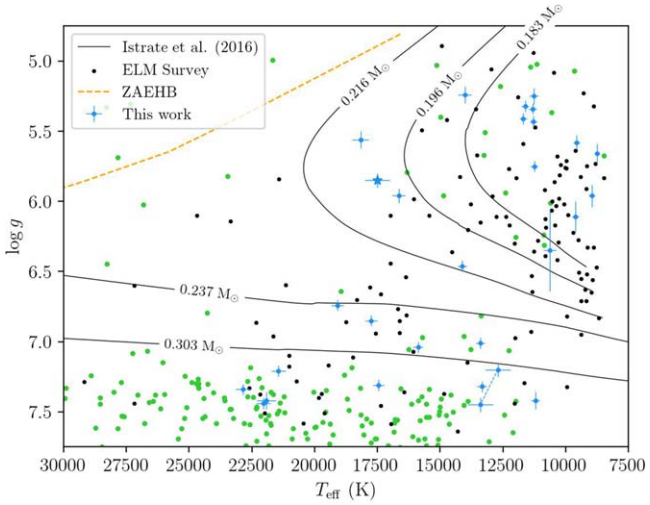

Figure 2. $\log g$–$T_{\rm eff}$ distribution of the low-mass white dwarfs identified as part of the ongoing ELM Survey. Previous ELM Survey binaries are displayed as black points. New binaries from this work are colored blue. Other objects observed as part of this work are colored green. We overplot the cooling tracks for 0.183 $M_\odot$, 0.196 $M_\odot$, 0.216 $M_\odot$, 0.237 $M_\odot$, and 0.303 $M_\odot$ white dwarfs with $Z = 0.001$ from Istrate et al. (2016), including rotation and diffusion. We mark the location of the DABZ J2049+3351 with a blue star symbol and use a dashed line to connect the markers for the individual stars in the double-lined binary J2102−4145. The zero-age extreme horizontal branch (ZAEHB) is colored as an orange dashed line for reference.

radius $R_2 = 0.0129\,R_\odot$, in agreement with the radius estimate from our light-curve modeling.

We similarly fit our eclipsing g- and r-band light curves for J0221+1710 separately using JKTEBOP (Southworth et al. 2004; Southworth 2013) to confirm the consistency of our LCURVE solution. We fit for the sum and ratio of the component radii, the inclination, and the surface brightness ratio. We performed 10,000 Monte Carlo iterations, which returned a solution degenerate in inclination ($88\overset{\circ}{.}6 \pm 0\overset{\circ}{.}2$ and $87\overset{\circ}{.}9 \pm 0\overset{\circ}{.}2$). The most-probable degenerate solution agrees well with our LCURVE results, returning $R_1 = 0.029 \pm 0.001\,R_\odot$, $R_2 = 0.013 \pm 0.001\,R_\odot$, $i = 88\overset{\circ}{.}6 \pm 0\overset{\circ}{.}2$, and $T_{\rm eff,2} \approx 6200$ K We report our simultaneous g- and r-band solution from the LCURVE solution as the true system parameters of J0221+1710.

With the individual component masses, orbital period, and orbital inclination known, we estimated the gravitational wave strain using the equation

$$h_c = 3.4 \times 10^{-23} \frac{\mathcal{M}^{5/3}\sqrt{\cos^4 i + 2\cos^2 i + 1}}{P^{2/3}\,d}, \quad (2)$$

where $\mathcal{M}$ is the chirp mass, P is the period in days, and d is the distance in kiloparsecs (Timpano et al. 2006; Roelofs et al. 2007). We multiplied by $\sqrt{(4\ {\rm yr}) f_{\rm GW}}$ to account for the increased signal after a 4 yr Laser Interferometer Space Antenna (LISA) mission. Our estimated gravitational wave strain for J0221+1710 is $h_c = (2.87 \pm 0.14) \times 10^{-20}$. Additionally, we estimated the orbital decay due to gravitational wave emission using the equation

$$\dot{P} = \frac{96}{5}\left(\frac{G\mathcal{M}}{P}\right)^{5/3}\frac{2\pi}{c^5}, \quad (3)$$

resulting in $\dot{P} = (3.86 \pm 0.14) \times 10^{-14}$ s s^{-1}, which corresponds to an eclipse timing offset of $\Delta T_0 \approx -3.6 \pm 0.1$ s after 10 yr.

6.3. J1121+6052

Our 26 radial velocity measurements of J112157.163+605210.265 (J1121+6052; GAIA DR3 861011995046220544) return best-fitting orbital parameters of $P_{\rm RV} = 2.0283 \pm 0.0003$ hr, $K = 183.5 \pm 2.6$ km s^{-1}, and $\gamma = -15.7 \pm 2.2$ km s^{-1}. We calculated the Galactic space velocities $[U,\ V,\ W] = [56.7 \pm 1.4,\ -10.2 \pm 1.5,\ 23.4 \pm 1.4]$ km s^{-1}, consistent with a short-period binary in the disk.

Our pure-hydrogen atmosphere fits to the summed zero-velocity spectrum of J1121+6052 resulted in atmospheric parameters of $T_{\rm eff} = 11{,}690 \pm 170$ K and $\log g = 5.41 \pm 0.05$, which suggests a white dwarf mass of $M_1 = 0.19 \pm 0.01\,M_\odot$ based on the Z = 0.02 model tracks of Istrate et al. (2016).

We find a weak periodic signal in the TESS 2 minutes cadence data through our LS periodicity search of J1121+6052 (TIC 417868394). The TESS light curve shows periodic variability at the 1% level with frequency $f_{\rm TESS} = 23.6649$ cycles day^{-1} ($P_{\rm TESS} = 1.0142$ hr), half the period obtained through the radial velocity measurements. We display the phase-folded TESS 2 minutes cadence light curve in Figure 3 (upper right). J1121+6042 is in a relatively isolated field, with no nearby bright stars to dilute the TESS light curve heavily. We do not recover this weak periodic signal in the available ground-based ZTF data.

6.4. J1506−1125

We obtained 31 radial velocity measurements for J150612.345−112511.994 (J1506−1125; Gaia DR3 6312837970697953920). Our best-fitting circular orbit fits suggest orbital parameters of $P_{\rm RV} = 0.7757 \pm 0.0094$ hr, $K = 167.5 \pm 4.3$ km s^{-1}, and $\gamma = 43.5 \pm 2.8$ km s^{-1}. J1506−1125 is likely a disk object with Galactic space velocities $[U,\ V,\ W] = [41.8 \pm 1.6,\ -7.3 \pm 1.5,\ 13.3 \pm 1.4]$ km s^{-1}.

Our pure-hydrogen model atmosphere fits to the summed zero-velocity spectrum result in best-fitting atmospheric parameters of $T_{\rm eff} = 22{,}050 \pm 320$ K and $\log g = 7.44 \pm 0.05$, which corresponds to a white dwarf with mass $M_1 = 0.43 \pm 0.02\,M_\odot$ based on the disk-metallicity models of Althaus et al. (2013). Our radial velocity measurements suggest a minimum companion mass of $M_{2,\rm min} = 0.18 \pm 0.01\,M_\odot$, significantly below the mass of the visible star.

Interestingly, our distance estimates suggest that J1506−1125 is overluminous when compared to our single-star spectral energy distribution (SED) models, which suggests that our single-star atmospheric model parameters may be inaccurate due to significant contribution to the system light from a companion. However, given the relatively low radial velocity semiamplitude ($K = 167.5 \pm 4.3$ km s^{-1}), we are not able to resolve individual absorption components in our Magellan 6.5 m optical spectrum with ≈1.0 Å resolution, if they are present.

We performed simultaneous model atmosphere fits to the SED and median-combined optical spectrum of J1506−1125, including contribution from two components in a binary (see Bédard et al. 2017; Kilic et al. 2020, for details of the method). The SED was built from the available near-UV (NUV) Galaxy Evolution Explorer (GALEX; Martin et al. 2005), SkyMapper (*uvgriz*; Onken et al. 2019), Pan-STARRS (*grizy*; Chambers et al. 2016), Two Micron All Sky Survey (2MASS, in

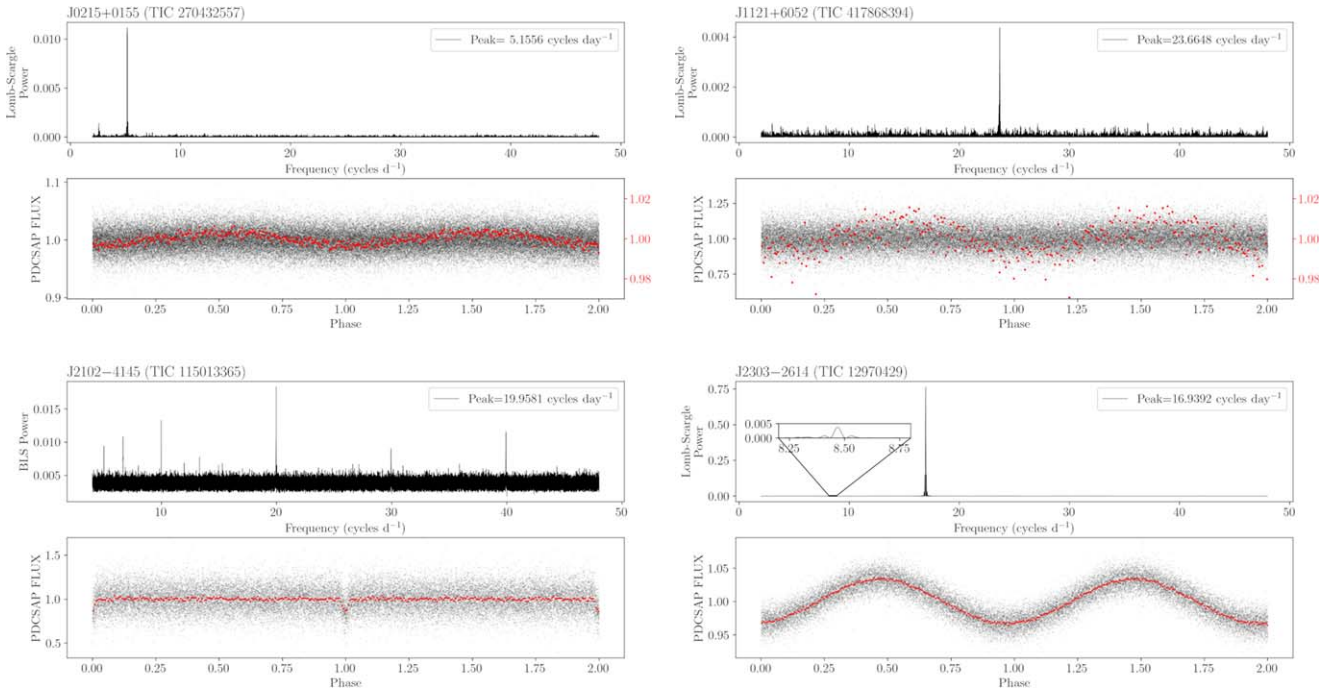

Figure 3. LS or BLS power spectrum (top) and its TESS 2 minutes cadence light curve (bottom) for J0215+0155 (TIC 270432557; upper left), J1121+6052 (TIC 417868394; upper right), J2102−4145 (TIC 115013365; lower left), and J2303−2614 (TIC 12970429; lower right). Red data points represent the original data binned by 100. We rescaled the binned data of J0215+0155 and J1121+6052 to emphasize the variability seen at the 1% level.

JHK$_s$; Skrutskie et al. 2006), and AllWISE (W1; Wright et al. 2010; Mainzer et al. 2011) photometry, and dereddened using the extinction maps of Schlafly & Finkbeiner (2011). Figure 5 shows the resulting χ^2 distribution plot as a function of $\log g_1$ and $\log g_2$, with the region of parameter space excluded by the constraints from the binary mass function shaded in blue. Dark regions indicate the regions with the most-probable system parameters based on our fits.

Because we do not resolve individual absorption components in our optical spectrum, we are unable to identify a unique solution to describe the atmospheric parameters of the components of J1506−1125. Figure 6 displays an example fit near the center of the dark region, defined by $T_{\rm eff,1} = 23{,}300$ K, $\log g_1 = 7.30$, $T_{\rm eff,2} = 18{,}300$ K, and $\log g_2 = 7.15$, corresponding to masses of $M_1 = 0.40\,M_\odot$ and $M_2 = 0.33\,M_\odot$ based on the He-core cooling tracks of Althaus et al. (2013). However, the extremes of our probable parameter space allow for solutions at $[(T_{\rm eff,1},\ T_{\rm eff,2}),\ (\log g_1,\ \log g_2),\ (M_1,\ M_2)] = [(22{,}000\ {\rm K},\ 18{,}100\ {\rm K}),\ (7.05,\ 7.55),\ (0.34\,M_\odot,\ 0.43\,M_\odot)]$ and $[(27{,}300\ {\rm K},\ 17{,}900\ {\rm K}),\ (7.80,\ 6.90),\ (0.54\,M_\odot,\ 0.28\,M_\odot)]$, where we used C/O-core cooling tracks of Bédard et al. (2020) for the relatively massive $0.54\,M_\odot$ solution.

We find no TESS FFI data, 2 minutes cadence data, or 20 s cadence data for J1506−1125 up to sector 56. Our LS and BLS algorithms do not identify periodic photometric variability in the public ZTF DR13 data archive.

6.5. J1812+0525

The orbital period of J181238.471+052529.868 (J1812+0525; Gaia DR3 4471573464995153280) was constrained through its periodic photometric variability identified in our search of the public ZTF data archive. Our LS periodogram identified periodic photometric variability at $P_{\rm ZTF} = 43.1$ minutes.

We obtained a single follow-up spectrum on 2022 June 3 to confirm its nature. We then completed its orbital solution with seven additional back-to-back spectra during the following night. Figure 7 (left) displays our orbital solution for J1812+0525. Our best-fitting radial velocity solution finds velocity semiamplitude $K = 373.3 \pm 6.2\ {\rm km\ s^{-1}}$, systemic velocity $\gamma = -139.6 \pm 4.7\ {\rm km\ s^{-1}}$, and orbital period $P_{\rm RV} = 1.436 \pm 0.002$ hr (86.2 ± 0.1 minutes), in good agreement with the half-period identified from the ZTF data. We use the precise Gaia DR3 astrometry, together with our radial velocity information, to estimate its Galactic velocities $[U,\ V,\ W] = [-92.9 \pm 2.3,\ -87.4 \pm 2.8,\ -1.1 \pm 2.4]\ {\rm km\ s^{-1}}$, which suggests that J1812+0525 is a short-period binary in the Galactic halo.

We fit the summed zero-velocity spectrum with pure-hydrogen model atmospheres and obtained best-fitting atmospheric parameters of $T_{\rm eff,0} = 9300 \pm 120$ K and $\log g_0 = 6.11 \pm 0.05$. Because this is a cool object, we corrected its atmospheric solution for 3D effects using the equations provided in Tremblay et al. (2015), resulting in corrected atmospheric parameters $T_{\rm eff} = 8960 \pm 130$ K and $\log g = 5.96 \pm 0.08$, corresponding to a primary mass of $M_1 = 0.28 \pm 0.03\,M_\odot$ based on the halo-metallicity models tracks of Istrate et al. (2016).

We used the McDonald Observatory 2.1 m telescope to confirm the photometric variability at $P = 43.4$ minutes, roughly consistent with the half-period seen in the public ZTF data. However, our data quality is too poor to constrain the orbital parameters reasonably through photometric fitting.

We instead modeled the ZTF DR16 *g*- and *r*-band data simultaneously using LCURVE. Our free parameters included the mass ratio ($q = \frac{M_1}{M_2} < 1.0$), scaled primary star radius ($r_1 = \frac{R_1}{a}$), orbital inclination (i), primary star effective temperature ($T_{\rm eff,1}$), time of superior conjunction (t_0), and the velocity scale (the sum of the unprojected orbital speeds). We fixed the

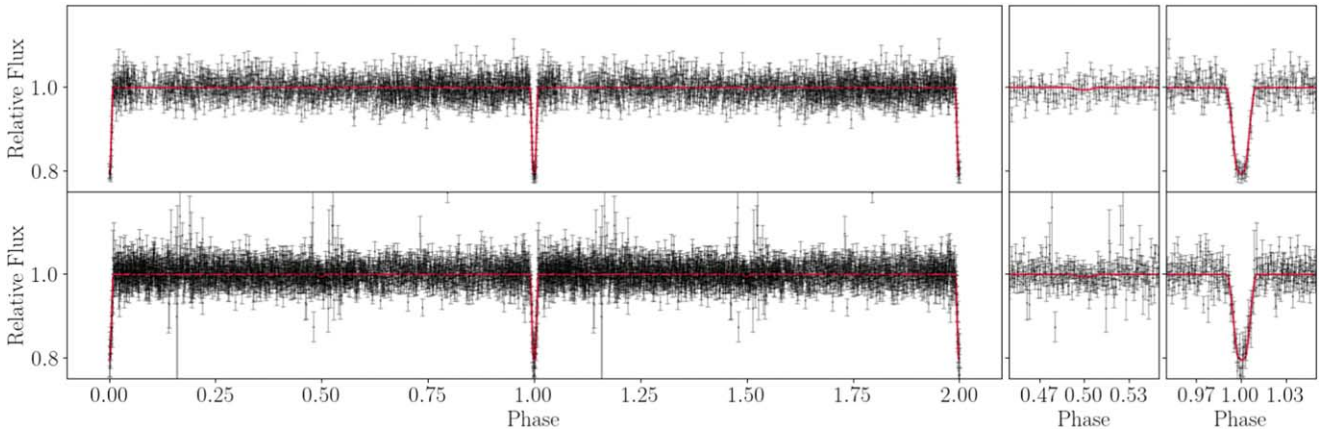

Figure 4. McDonald 2.1 m *g*-band (top) and *r*-band (bottom) light curves of J0221+1710. Best-fitting LCURVE models are overplotted in red. We provide zoomed-in subplots showing the regions surrounding the primary and secondary eclipses.

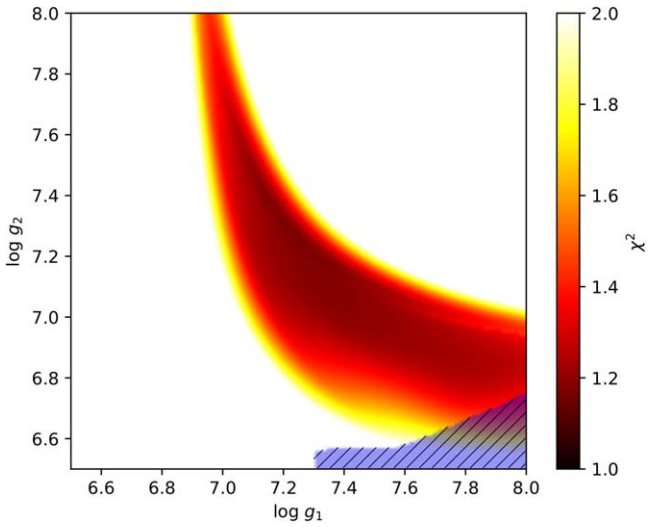

Figure 5. Normalized χ^2 distribution from our fits to the combined SED and optical spectroscopy for J1506−1125, as a function of $\log g_1$ and $\log g_2$. The hatched blue region represents the region of parameter space excluded by the constraints from the binary mass function.

gravity and quadratic limb-darkening coefficients to the values from Claret et al. (2020) for a $T_{\rm eff,1} = 9000$ K, $\log g_1 = 6.0$ primary with a $T_{\rm eff,2} = 5500$ K, $\log g_1 = 8.0$ companion and assign Gaussian priors based on our spectroscopic values for $T_{\rm eff,1}$, $\log g_1$, and K_1. The most-probable system parameters based on our light-curve modeling are $q = 0.42 \pm 0.03$, $r_1 = 0.20 \pm 0.01$, $i = 75^{+2}_{-5}{}^{\circ}$, and $T_{\rm eff,1} = 8900 \pm 100$ K. These parameters are summarized in Table 3. With the constraints from our radial velocity measurements, this corresponds to an $M_1 = 0.30 \pm 0.03\,M_\odot$ primary star with an $M_2 = 0.73^{+0.05}_{-0.04}\,M_\odot$ companion.

6.6. J2049+3351

The orbital period of J204951.274+335153.126 (J2049+3351; Gaia DR3 1869111286948848128) was constrained through its periodic photometric variability identified in our search of the public ZTF data archive. Our LS algorithm identified strong variability at $P_{\rm ZTF} = 21.6$ minutes with amplitude $A \approx 0.07$ mag.

We obtained a single follow-up spectrum on 2022 June 3 to confirm its nature and completed its orbital solution with seven additional back-to-back spectra on the following night. Figure 7 (right) displays our orbital solution for J2049+3351. Our best-fitting radial velocity solution yields velocity semiamplitude $K = 513.2 \pm 9.5$ km s^{-1}, systemic velocity $\gamma = -3.4 \pm 7.7$ km s^{-1}, and orbital period $P_{\rm RV} = 0.7139 \pm 0.0002$ hr (42.834 ± 0.012 minutes), in good agreement with the half-period identified from the ZTF data. The Galactic space velocities, $[U,\ V,\ W] = [-9.8 \pm 2.4,\ -8.1 \pm 2.6,\ 13.4 \pm 2.3]$ km s^{-1}, place J2049+3351 in the Galactic disk.

J2049+3351 has an interesting optical absorption spectrum, including broad hydrogen Balmer lines with strong He I absorption at 4472 Å, 4388 Å, 4143 Å, and 4026 Å, as well as a weak Ca II feature at 3933 Å. Our MMT 6.5 m optical spectrum of J2049+3351 is presented in Figure 8. We note that the individual hydrogen and helium absorption lines appear to move in sync with each other throughout the orbit of the binary.

To fit the coadded spectrum of J2049+3351, we use spectral models which were constructed using the hybrid LTE/NLTE approach described in detail in Przybilla et al. (2011) and Irrgang et al. (2021). The grid of spectral models covers a typical range of hot subdwarf $T_{\rm eff}$ and $\log g$, up to modest helium abundances (Irrgang et al. 2021, 2022; Heber 2023). Our best-fitting parameters, with their bootstrapped uncertainties, are $T_{\rm eff} = 17{,}500 \pm 500$ K, $\log g = 5.85 \pm 0.05$, $\log \frac{\rm He}{\rm H} = -0.24 \pm 0.07$, and $v_{\rm rot} = 260 \pm 60$ km s^{-1}. Best-fitting solutions without rotational broadening fail to reproduce the observed broad helium absorption lines. We present the best-fitting model atmosphere overplotted on our optical spectrum in Figure 9.

We obtained 218 minutes of *g*-band and 108 minutes of *r*-band high-speed photometry using the McDonald 2.1 m telescope. We performed a simultaneous multiband fit to our unbinned light curves using LCURVE. We assign the time of primary conjunction using our radial velocity data and fit for the mass ratio, individual stellar radii, orbital inclination, and effective temperatures.

Our best-fitting model identifies primary and secondary eclipses in the data. However, J2049+3351 is faint (Gaia G = 18.7 mag), and our 2.1 m McDonald light curves are noisy. While the eclipses are not seen in our *r*-band light curve due to the high noise level, a relatively clean secondary-eclipse

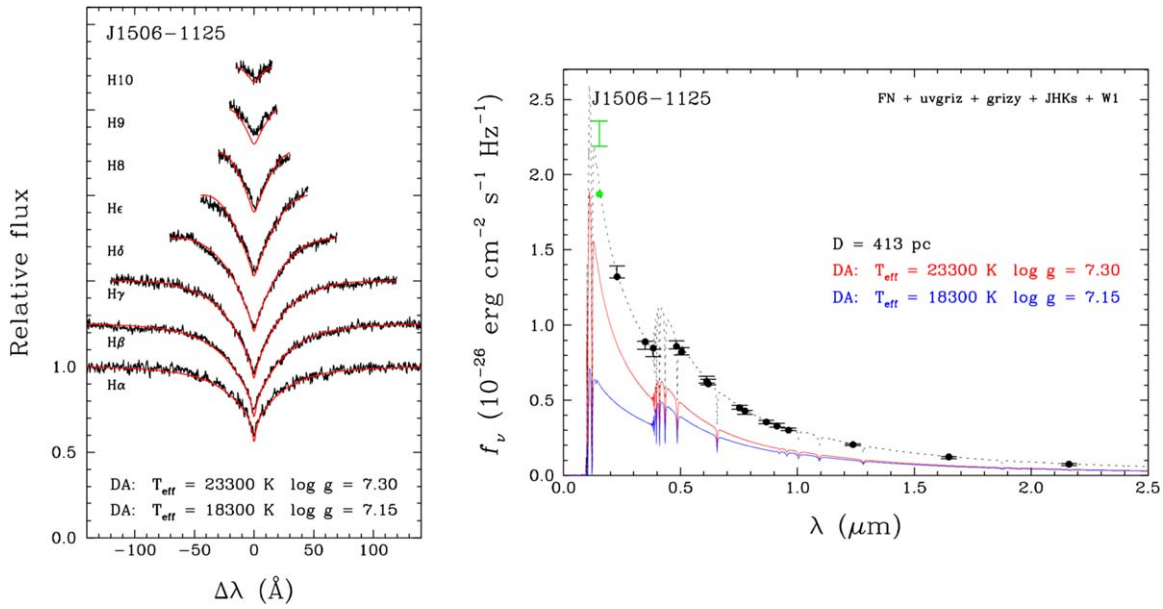

Figure 6. Example model atmosphere fit to the spectrum (left) and SED (right) of J1506−1125, including contributions from two DA white dwarfs. In the left panel, the observed and predicted Balmer lines are shown as black and red lines, respectively. In the right panel, the observed and predicted average fluxes are displayed as error bars and filled circles, respectively; for reference, the red and blue lines show the individual contributions of the components to the total monochromatic model flux, which is displayed as a black dotted line. The GALEX FUV photometry measurement (green) is excluded from our SED fit. This fit does not represent a unique solution (see text).

feature can be seen in the binned g-band light-curve data and a noisy primary-eclipse feature may be visible in our unbinned g-band data. We present our binned and phase-folded McDonald 2.1 m g- and r-band light curves in Figure 10 with the most-probable light-curve model overplotted as a red line and radial velocity curve overplotted in blue.

Our best-fitting model to the McDonald 2.1 m light curves finds mass ratio $q = \frac{M_1}{M_2} = 0.39 \pm 0.2$, inclination $i = 74° \pm 3°$, $T_{\rm eff,1} = 23,200^{+4900}_{-4300}$ K, $T_{\rm eff,2} = 35,400^{+9700}_{-8600}$ K, $r_1 = \frac{R_1}{a} = 0.31 \pm 0.05$, and $r_2 = \frac{R_2}{a} = 0.06^{+0.03}_{-0.02}$. We summarize these values in Table 3.

Because J2049+3351 is faint, large-aperture high-speed photometry will be required to obtain a sufficient S/N to confirm the presence of eclipses. These future observations will be used to place precise constraints on the binary parameters and determine the evolutionary history of J2049+3351.

6.7. J2102−4145

J210220.456−414501.736 (J2102−4145; Gaia DR3 6581249825853801984) is a relatively bright (Gaia G = 15.7 mag) and nearby ($d_\pi = 165 \pm 1$ pc) eclipsing low-mass white dwarf binary. Our 6.5 m Magellan spectroscopic follow-up observations reveal two nearly equal-depth absorption components, most easily seen in Hα. Thus J2102−4145 is now the eighth confirmed double-lined, double-degenerate, eclipsing white dwarf binary published after CSS41177 (J1005+2249; Bours et al. 2014), ZTF J1539+5027 (Burdge et al. 2019), ZTF J1901+5309 (Coughlin et al. 2020), and ZTF J0538+1953, ZTF J0722−1839, ZTF J1749+0924, and ZTF J2029+1534 (Burdge et al. 2020).

Because the individual absorption components are roughly equal depth, obtaining a precise orbital period and individual velocity semiamplitudes leads to significant period aliases when combining data over multiple nights. Our 55 radial velocity measurements for J2102−4145 provide orbital period constraints with strong period aliases between $P_{\rm RV} = 2-3$ hr.

Fortunately, the TESS 2 minutes cadence data archive provides a light curve for J2102−4145 (TIC 115013365). Our BLS algorithm identifies periodic eclipses in the TESS light curve with period $P_{\rm BLS} = 1.2$ hr, with its phase-folded light curve showing a shallow primary eclipse heavily diluted by a bright (Gaia $G = 11.2$ mag) field star roughly 30″ away. Figure 3 (lower left) shows the phase-folded TESS 2 minutes cadence light curve and its BLS periodogram for J2102−4145.

Given that this is a double-lined spectroscopic binary with nearly equal-depth absorption components, our BLS algorithm will confuse the nearly equal-depth primary and secondary eclipses at the true orbital period with one primary eclipse occurring twice as often. Our BLS algorithm has identified the half-period; the true orbital period of J2102−4145 is therefore $P = 2.4$ hr, in agreement with the constraints from our radial velocity analysis.

Using the TESS period, we were able to constrain the orbital solutions for both stars in the binary. Figure 12 displays our best-fitting orbital solution for each star, using data from Magellan and Gemini South. We find $P_{\rm RV} = 144.3^{+0.4}_{-0.3}$ minutes, $K_1 = 227 \pm 8$ km s^{-1}, $\gamma_1 = -8^{+7}_{-6}$ km s^{-1}, $K_2 = 186 \pm 8$ km s^{-1}, and $\gamma_2 = -19^{+6}_{-7}$ km s^{-1}, corresponding to binary mass ratio $q = 0.82 \pm 0.05$.

Finally, we performed simultaneous model atmosphere fits to the SED and median-combined spectrum of J2102−4145, including the contributions of both components. To avoid significant smearing, our median-combined spectrum used four consecutive spectra covering 9% of the orbit, approaching maximum separation. Our fits also made use of the Gaia DR3 parallax measurement and the mass ratio constraint provided by the orbital solution, thanks to which we were able to obtain a unique solution, shown in Figure 11.

Our best-fitting solution suggests that J2102−4145 contains two similar DA white dwarfs with atmospheric parameters

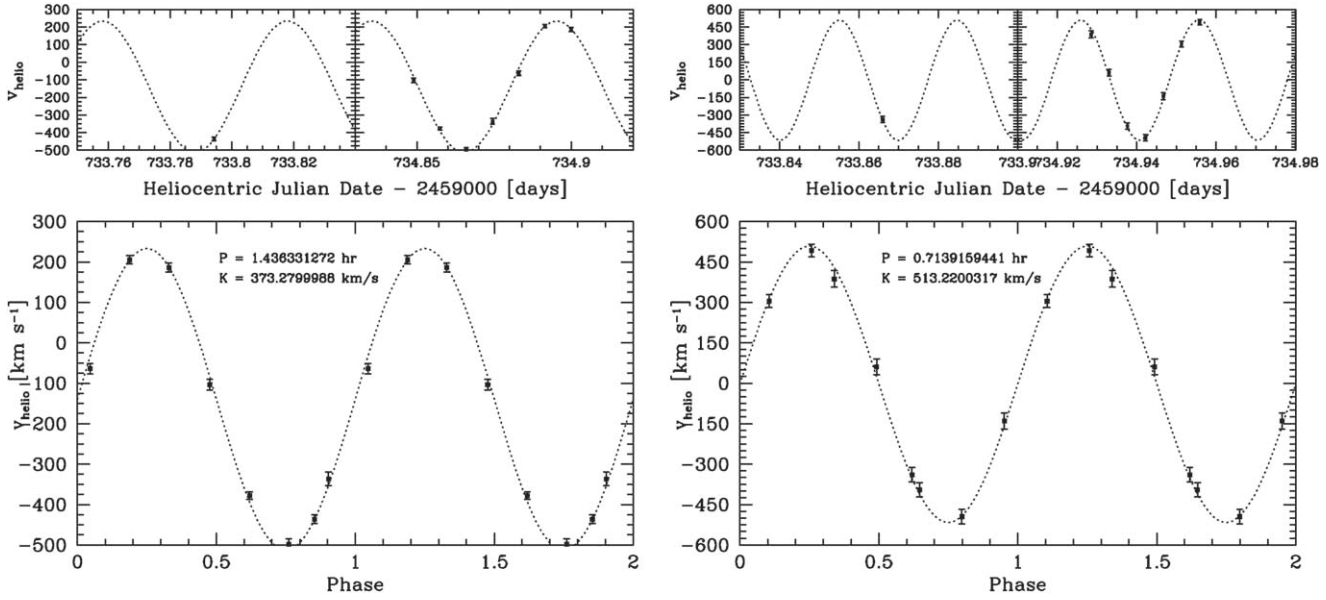

Figure 7. Orbital solutions for J1812+0525 (left) and J2049+3351 (right).

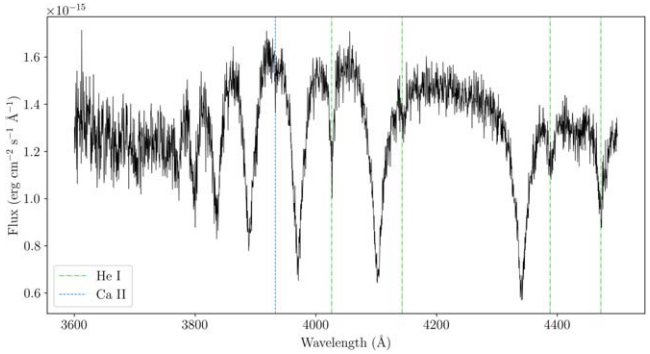

Figure 8. Coadded MMT optical spectrum of J2049+3351. In addition to the dominant hydrogen Balmer absorption, strong neutral helium absorption features (green dashed–dotted lines) can be seen at 4472 Å, 4388 Å, 4143 Å, and 4026 Å, as well as a weak Ca II absorption feature (blue dash lines) at 3933 Å.

$T_{\rm eff,1} = 12{,}700 \pm 500$ K, $\log g_1 = 7.20 \pm 0.05$, $T_{\rm eff,2} = 13{,}400 \pm 500$ K, and $\log g_2 = 7.45 \pm 0.05$, corresponding to masses of $M_1 = 0.32\,M_\odot$ and $M_2 = 0.39\,M_\odot$ based on the He-core white dwarf tracks of Althaus et al. (2013), in agreement to within 2σ of the expected values based on the difference in systemic velocities measured from our radial velocity solution.

High-speed light-curve follow up of J2102−4145 will allow for a rare opportunity to measure the radii of the individual stars in the binary directly, independent of model estimates.

6.8. J2303−2615

We obtained 34 radial velocity measurements of J230323.542−261459.917 (J2303−2614; Gaia DR3 2382531303846872448), resulting in a best-fitting circular orbit with parameters $P_{\rm RV} = 2.8367 \pm 0.0008$ hr, $K = 302.9 \pm 2.3$ km s^{-1}, and $\gamma = -17.1 \pm 2.1$ km s^{-1}. J2303−2614 is a disk object with $[U, V, W] = [31.1 \pm 1.2, -60.0 \pm 1.4, 18.8 \pm 1.4]$ km s^{-1}.

We fit the median-combined zero-velocity spectrum with pure-hydrogen atmosphere models and obtained best-fitting atmospheric parameters of $T_{\rm eff} = 11{,}280 \pm 170$ K and

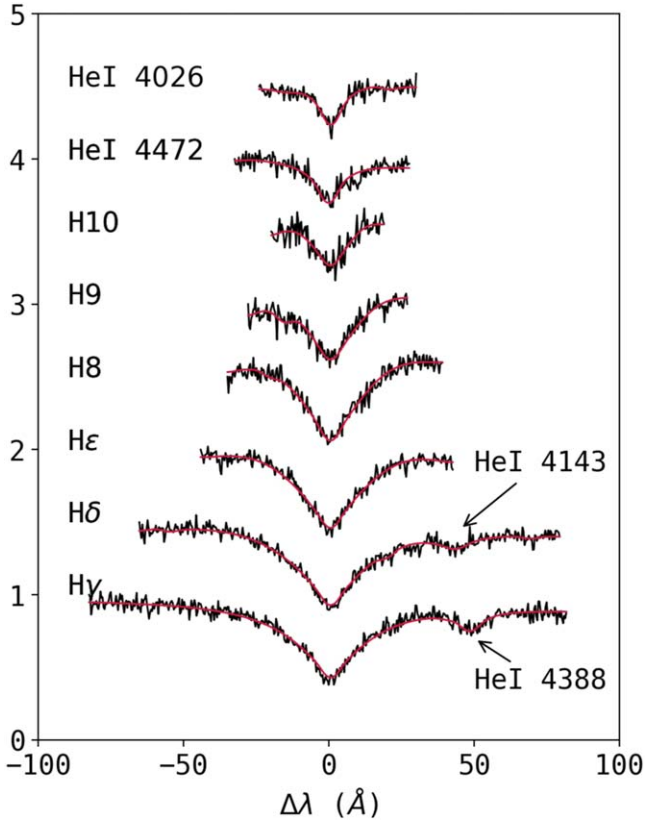

Figure 9. Best-fitting spectroscopic model to the optical spectroscopy of J2049+3351, including rotational broadening.

$\log g = 5.43 \pm 0.05$, corresponding to a white dwarf with mass $M_1 = 0.18 \pm 0.01\,M_\odot$.

Our LS periodogram identified strong periodic photometric variability in the TESS 2 minutes cadence data of J2303−2614 (TIC 12970429) at frequency $f_{\rm TESS} = 16.9392$ cycles day^{-1} ($P = 1.417$ hr), in good agreement with half the orbital period seen in our radial velocity follow up, suggesting that J2303−2614 is another tidally distorted white dwarf in a compact

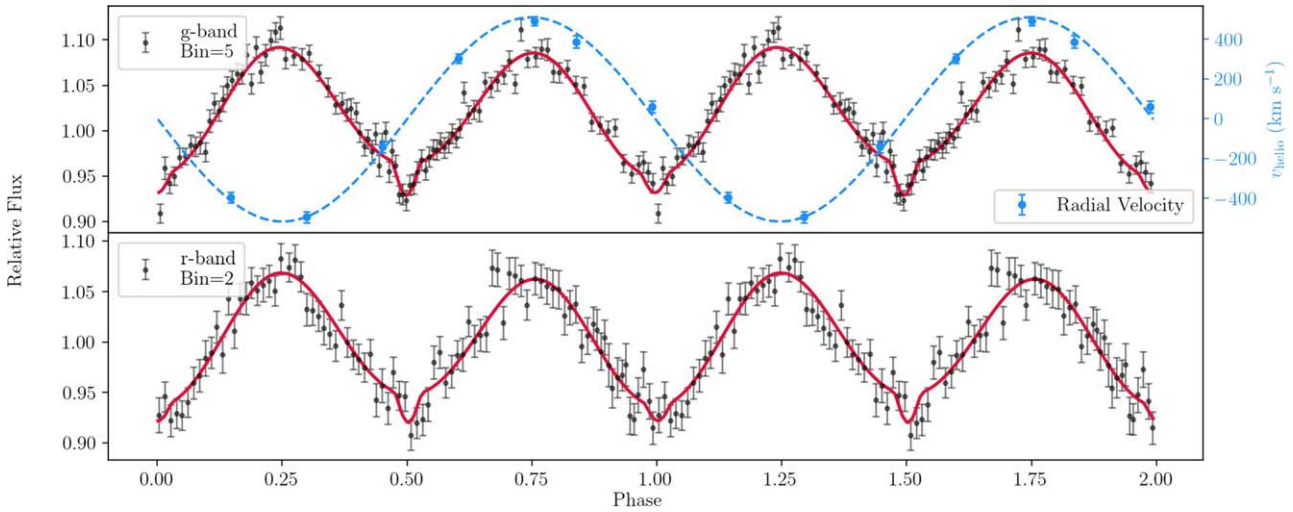

Figure 10. Top: McDonald 2.1 m *g*-band (top; binned by 5) and *r*-band (bottom; binned by 2) light curves of ZTF J2049+3351. We overplot our radial velocity measurements as blue data points in the top panel.

binary. Figure 3 (lower right) shows the phase-folded TESS 2 minutes cadence light curve and its LS power spectrum. We provide a zoomed inset plot showing a small, but significant, peak at the true orbital period of this system.

7. Discussion

7.1. Detectable LISA Binaries

General relativity predicts that the orbits of compact binaries decay due to the emission of gravitational waves. Binaries with orbital periods $P \lesssim 6$ hr will merge within a Hubble time. The shortest period white dwarf binaries, with periods $P \lesssim 1$ hr, will be the dominant source of gravitational wave signal for the LISA mission (Amaro-Seoane et al. 2017), creating an incoherent noise floor in the LISA sensitivity range at milliHertz frequencies (Nelemans et al. 2001; Korol et al. 2017; Li et al. 2020; Amaro-Seoane et al. 2023).

Over 40 compact binaries have been characterized through their electromagnetic radiation and will be individually resolved by LISA, many of which will act as verification binaries for the LISA mission data calibration (see Finch et al. 2023; Kupfer et al. 2023, and references therein). These individually resolvable gravitational wave binaries will provide a multimessenger approach to studying compact binary evolution through their electromagnetic and gravitational wave emission. We find that two of our 28 new binaries will be detected by LISA within a 4 yr mission.

Our single-star spectroscopic fits to J1506−1125 suggests that it contains an $M_1 = 0.43 \pm 0.02\,M_\odot$ white dwarf in a $P = 0.7757 \pm 0.0094$ hr binary with an $M_2 > 0.18 \pm 0.01\,M_\odot$ companion at a distance of $d_\pi = 413 \pm 18$ pc. We used the NASA LISA Detectability Calculator[13] to estimate its expected LISA S/N over 4 yr of observation to be S/N = 1.9 assuming $i = 90°$, or S/N = 3.7 assuming $i = 60°$. However, our single-component fits to the SED of J1506−1125 suggests significant contribution to the total system light from an unseen companion. Our simultaneous multicomponent fits to the available SED and optical spectroscopy of J1506−1125 (discussed in Section 6) suggest a large range of probable stellar parameters for each component. Over this range, we find S/Ns between 3.9 and 4.7 assuming $i = 90°$, or 6.1–7.3 assuming $i = 60°$.

J152601.115−271156.660 (J1526−2711; Gaia DR3 6213619999912198144) is a $P = 0.67 \pm 0.01$ hr binary containing an $M_1 = 0.37 \pm 0.02\,M_\odot$ primary with an $M_2 > 0.40 \pm 0.02\,M_\odot$ companion at a distance $d_\pi = 623 \pm 68$ pc. J1526−2711 is a detectable LISA binary with a 4 yr S/N = 3.3 assuming $i = 90°$, or S/N = 6.4 assuming $i = 60°$.

We find no photometric variability for either of these binaries in the public ZTF and TESS data archives. LISA detections will provide precise constraints to their orbital inclinations and chirp masses, which will be used to constrain the individual component masses directly, leading to estimates on the eventual merger outcomes.

Figure 13 displays the LISA 4 yr sensitivity curve for the ELM Survey binaries (black) with the 28 new binaries presented here (blue). We calculated the gravitational wave strain for each of our new binaries using Equation (2), assuming $i = 90°$ if the orbital inclination was not known through photometric constraints.

7.2. Comparison with Other Surveys

Pelisoli & Vos (2019) created a catalog of 5672 ELM white dwarf candidates based on Gaia DR2 astrometry with extensive target cuts to remove contamination. We cross-matched our 28 new binaries with the Gaia DR2 ELM white dwarf candidate catalog of Pelisoli & Vos (2019) and find 13 matches, which we mark in Tables 1 and 2. Many of the remaining binaries not reported as ELM white dwarf candidates in Pelisoli & Vos (2019) were excluded in their color cuts used to remove cataclysmic variables and white dwarf + M dwarf binary contaminants.

Wang et al. (2022) used LAMOST DR8 low-resolution spectroscopy to refine the candidate list of Pelisoli & Vos (2019) further and identified 21 high-probability ELM white dwarfs based on spectroscopic fits to the low-resolution LAMOST data, including two of the new binaries we present in this work. Wang et al. (2022) identified J0215+0155 with atmospheric parameters of $T_{\rm eff} = 10{,}540 \pm 40$ K and

[13] https://heasarc.gsfc.nasa.gov/lisa/lisatool/

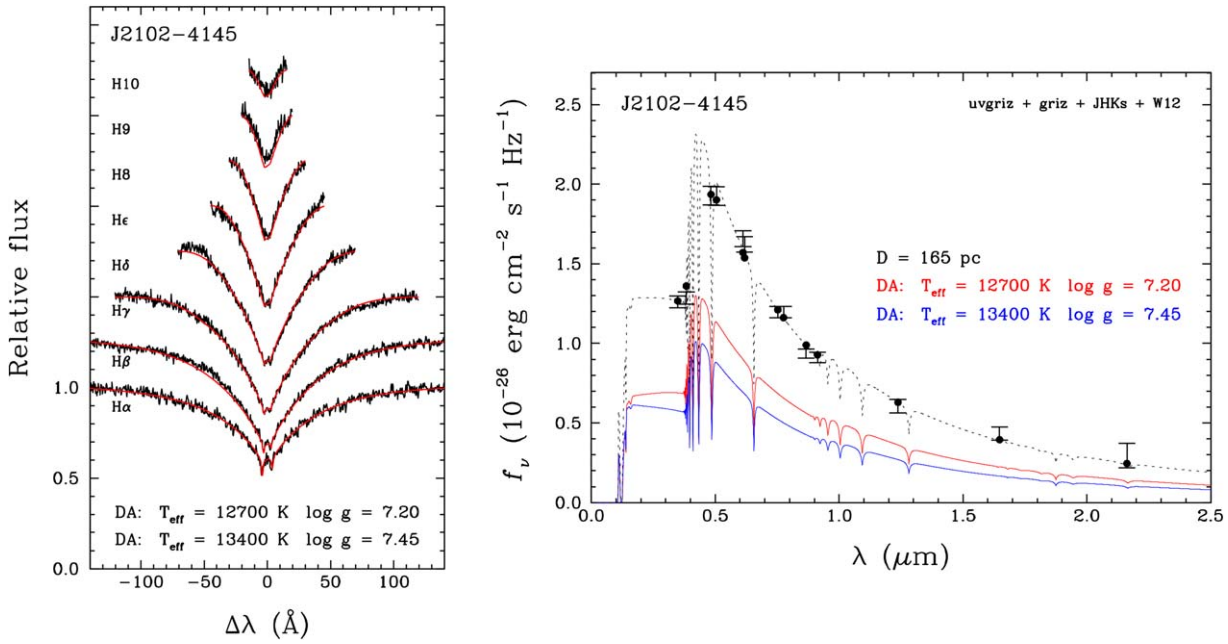

Figure 11. Best simultaneous model atmosphere fit to the spectrum (left) and SED (right) of J2102−4145 including contributions from two DA white dwarfs. In the left panel, the observed and predicted Balmer lines are shown as black and red lines, respectively. In the right panel, the observed and predicted average fluxes are displayed as error bars and filled circles, respectively; for reference, the red and blue lines show the individual contributions of the components to the total monochromatic model flux, which is displayed as a black dotted line.

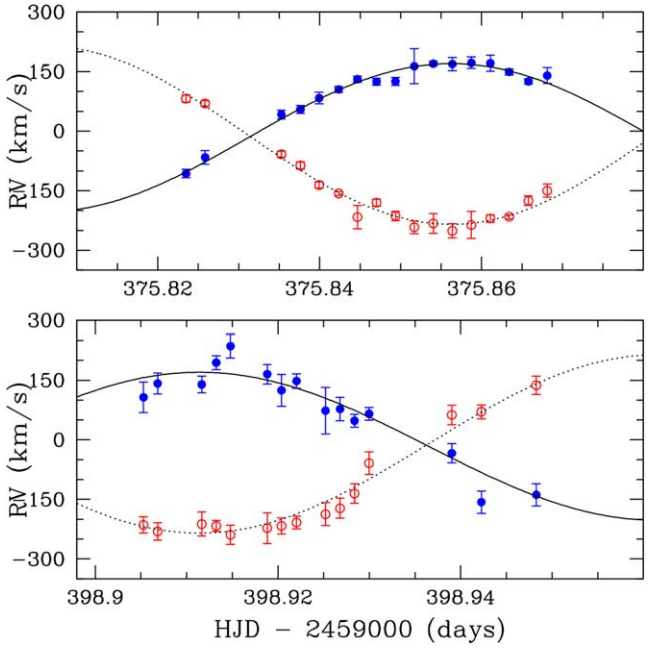

Figure 12. Orbital solutions for each component of the double-lined binary J2102−4145. Top: Magellan 6.5 m telescope data. Bottom: Gemini South 8.1 m telescope data. The blue/red points represent the radial velocity measurements for the primary/secondary star.

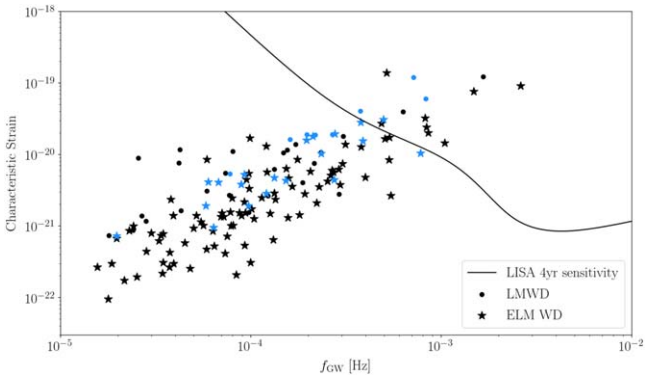

Figure 13. Four-year LISA sensitivity plot including the white dwarf binaries identified as part of the ELM Survey (black) and the 28 new white dwarf binaries from this work (blue). ELM white dwarfs ($M \leqslant 0.305\ M_{\odot}$) are marked as star symbols while low-mass white dwarfs are marked as circles.

$\log g = 5.06 \pm 0.07$, significantly lower than the values we find for our combined spectrum. Additionally, the authors identify significant radial velocity variability in two spectra of J1129+4715, with $T_{\rm eff,1} = 11{,}670 \pm 50$ K, $\log g_1 = 5.31 \pm 0.06$, and $v_{\rm rad,1} = -38.9 \pm 3.0\ {\rm km\ s^{-1}}$ and $T_{\rm eff,2} = 11{,}150 \pm 90$ K, $\log g_2 = 5.06 \pm 0.02$, and $v_{\rm rad,2} = 94.9 \pm 5.4\ {\rm km\ s^{-1}}$, the first of which is in excellent agreement with the atmospheric parameter estimates from the fits presented in this work.

7.3. Conclusions

This work has identified 28 new low-mass white dwarf binaries, bringing the total number of ELM Survey binaries to 148, with 41 located in the southern sky. Interestingly, this work identifies only three halo binaries among our 28 new binaries (≈11%). Previous ELM Survey results suggest a significant contribution from halo objects of ≈30%–40% (Gianninas et al. 2015; Brown et al. 2022), likely due to the early ELM Survey target selection being based on photometry from SDSS, which observed at high Galactic latitudes. Additionally, our low fraction of new halo objects is likely affected by our Gaia-based selection, and in-progress object follow up favoring nearby objects with reliable parallax measurements, rather than more distant halo objects.

Large-scale time domain surveys are an excellent tool for the discovery of photometrically variable systems. Burdge et al. (2020)

Table 2
Orbital Solutions to the 28 New Low-mass White Dwarf Binaries Presented in This Work

Object Name	P (days)	K (km s^{-1})	γ (km s^{-1})	M_2 ($M_\odot$)	$\tau_{\rm merge}$ (Gyr)	Disk
J0135+2359	1.177655 ± 0.009923	178.9 ± 6.4	−35.7 ± 6.2	>1.02 ± 0.09	<371.4 ± 71.7	1
J0155−4148	0.343865 ± 0.000317	220.4 ± 3.7	−4.0 ± 2.9	>0.67 ± 0.03	<18.1 ± 1.6	1
J0215+0155[c]	0.387941 ± 0.000001	186.4 ± 1.5	−49.4 ± 1.1	>0.58 ± 0.02	<21.7 ± 1.4	0
J0221+1710[c]	0.061288 ± 0.000020	347.9 ± 4.2	35.3 ± 3.7	0.58 ± 0.02	0.17 ± 0.01	1
J0256+4405	0.261260 ± 0.000087	243.7 ± 3.8	28.1 ± 2.9	>0.68 ± 0.03	<8.6 ± 0.8	1
J0450−0145[c]	0.192169 ± 0.000040	260.2 ± 3.3	65.5 ± 2.9	>0.61 ± 0.02	<4.7 ± 0.5	1
J0501−2312[c]	0.086593 ± 0.001156	105.1 ± 5.1	6.3 ± 7.2	>0.14 ± 0.01	<1.1 ± 0.1	1
J0517−1153[c]	0.250521 ± 0.000001	309.7 ± 3.1	53.5 ± 2.6	>1.07 ± 0.04	<6.3 ± 0.7	1
J0545−1902	0.144472 ± 0.000684	134.7 ± 5.4	146.1 ± 5.7	>0.25 ± 0.02	<2.4 ± 0.2	1
J0725−1245	0.106135 ± 0.000061	79.6 ± 5.0	90.4 ± 3.2	>0.12 ± 0.01	<2.0 ± 0.2	1
J1121+6052[a]	0.084511 ± 0.000013	183.5 ± 2.6	−15.7 ± 2.2	>0.20 ± 0.01	<1.3 ± 0.1	1
J1129+4715[c]	0.238823 ± 0.000032	185.8 ± 4.4	40.9 ± 3.0	>0.37 ± 0.02	<12.4 ± 0.7	1
J1240−0958	0.400383 ± 0.002945	209.8 ± 6.1	23.9 ± 3.3	>0.65 ± 0.04	<30.3 ± 3.2	1
J1255−1853	0.363739 ± 0.001501	230.8 ± 6.2	−15.2 ± 29.5	>0.73 ± 0.04	<22.6 ± 1.5	1
J1459−1920	0.151990 ± 0.000030	287.8 ± 7.4	45.6 ± 5.0	>0.70 ± 0.04	<1.7 ± 0.1	0
J1506−1125	0.032320 ± 0.000390	167.5 ± 4.3	43.5 ± 2.8	>0.18 ± 0.01	<0.056 ± 0.003	1
J1526−2711[c]	0.027982 ± 0.000439	336.0 ± 5.6	8.4 ± 4.8	>0.40 ± 0.02	<0.021 ± 0.001	1
J1553+6736[c]	0.174522 ± 0.000431	91.6 ± 5.4	10.9 ± 6.1	>0.12 ± 0.01	<12.4 ± 2.3	1
J1555+1007[c]	0.298037 ± 0.000877	148.5 ± 6.7	−51.4 ± 3.7	>0.38 ± 0.03	<13.0 ± 1.0	1
J1657−0417	0.083954 ± 0.000441	289.4 ± 8.8	−69.8 ± 21.3	>0.50 ± 0.03	<0.44 ± 0.04	1
J1808+2723	0.098787 ± 0.000053	187.2 ± 3.0	−69.3 ± 1.9	>0.24 ± 0.02	<1.4 ± 0.2	1
J1812+0525[b]	0.059847 ± 0.000083	373.3 ± 6.2	−139.6 ± 4.7	$0.73^{+0.05}_{-0.04}$	0.13 ± 0.01	0
J1832+2031[c]	0.046641 ± 0.000002	335.2 ± 4.2	−37.4 ± 3.3	>0.47 ± 0.02	<0.090 ± 0.009	1
J2013−1310[c]	0.061618 ± 0.000597	300.9 ± 6.5	−40.2 ± 6.3	>0.51 ± 0.02	<0.14 ± 0.01	1
J2049+3351[b]	0.029747 ± 0.000007	513.2 ± 9.5	−3.4 ± 7.7	⋯	⋯	1
J2102−4145a[a]	0.117631 ± 0.003244	227^{+8}_{-6}	$-7.9^{+7.1}_{-5.8}$	⋯	<0.74 ± 0.02	1
J2102−4145b[a]	0.117631 ± 0.003244	186^{+8}_{-7}	$-18.7^{+6.2}_{-7.0}$	⋯	<0.74 ± 0.02	1
J2243−4511	0.109479 ± 0.000043	249.4 ± 4.9	6.0 ± 3.7	>0.46 ± 0.02	<0.89 ± 0.04	1
J2303−2614[a,c]	0.118195 ± 0.000032	302.9 ± 2.3	−17.1 ± 2.1	>0.58 ± 0.01	<1.4 ± 0.1	1

Notes.
[a] Photometric variability: TESS high cadence.
[b] Photometric variability: ZTF.
[c] Pelisoli & Vos (2019) ELM white dwarf candidate.

(This table is available in machine-readable form.)

Table 3
System Parameters for J0211+1710, J1812+0525, and J2049+3351 Obtained Through Light-curve Modeling with LCURVE as Described in the Text

	J0221+1710	J1812+0525	J2049+3351
q	⋯	0.41 ± 0.03	0.39 ± 0.2
i (°)	89.0 ± 0.2	75^{+2}_{-5}	74^{+3}_{-2}
R_1/a	0.045 ± 0.001	0.20 ± 0.01	0.31 ± 0.05
R_2/a	0.020 ± 0.001	⋯	$0.06^{+0.03}_{-0.02}$
$T_{\rm eff,1}$ (K)	13,400 ± 180	8900 ± 100	$23{,}200^{+4900}_{-4300}$
$T_{\rm eff,2}$ (K)	$\lesssim$6400	⋯	$35{,}400^{+9700}_{-8600}$

identified 15 ultracompact ($P < 1$ hr) binaries which show photometric variability in the ZTF data archive. We used the ZTF and TESS data archives to identify photometric variability in seven of our new binaries, including three short-period eclipsing binaries. These short-period eclipsing binaries are especially important for determining the precise physical parameters of both stars in the binary, which are valuable for binary population studies. Similar upcoming large-scale time domain surveys, such as BlackGEM (Bloemen et al. 2015), and the Vera C. Rubin Observatory's Legacy Survey of Space and Time (LSST) program (Ivezić et al. 2019) will enable efficient identification and characterization of white dwarf binaries in the southern sky, which will quickly expand the known population of ELM white dwarf binaries and allow for a more detailed population study of all-sky ELM white dwarf binaries.

Acknowledgments

A.K. acknowledges support from NASA through grant 80NSSC22K0338.

M.K. acknowledges support from the National Science Foundation (NSF) under grants AST-1906379 and AST-2205736, and NASA under grant 80NSSC22K0479.

T.K. acknowledges support from the NSF through grant AST #2107982, from NASA through grant 80NSSC22K0338, and from the Space Telescope Science Institute (STScI) through grant HST-GO-16659.002-A.

M.A.A. acknowledges support from a Fulbright U.S. Scholar grant cofunded by the Nouvelle-Aquitaine Regional Council and the Franco-American Fulbright Commission. M.A.A. also acknowledges support from a Chrétien International Research Grant from the American Astronomical Society.

We would like to thank Ulrich Heber and Andreas Irrgang for the providing the spectral models for J2049+3351.

We thank the anonymous referee for helpful comments and suggestions that improved the quality of this work.

This work has made use of data from the European Space Agency (ESA) mission Gaia (https://www.cosmos.esa.int/gaia), processed by the Gaia Data Processing and Analysis Consortium (DPAC; https://www.cosmos.esa.int/web/gaia/dpac/consortium). Funding for the DPAC has been provided by national institutions, in particular the institutions participating in the Gaia Multilateral Agreement.

Based on observations obtained at the international Gemini Observatory, a program of NSF's NOIRLab, which is managed by the Association of Universities for Research in Astronomy (AURA) under a cooperative agreement with the National Science Foundation on behalf of the Gemini Observatory partnership: the National Science Foundation (United States), National Research Council (Canada), Agencia Nacional de Investigación y Desarrollo (Chile), Ministerio de Ciencia, Tecnología e Innovación (Argentina), Ministério da Ciência, Tecnologia, Inovações e Comunicações (Brazil), and Korea Astronomy and Space Science Institute (Republic of Korea).

Based on observations obtained at the Southern Astrophysical Research (SOAR) telescope, which is a joint project of the Ministério da Ciência, Tecnologia e Inovações do Brasil (MCTI/LNA), the US National Science Foundation's NOIRLab, the University of North Carolina at Chapel Hill (UNC), and Michigan State University (MSU).

Observations reported here were obtained at the MMT Observatory, a joint facility of the Smithsonian Institution and the University of Arizona.

The MDM Observatory is operated by Dartmouth College, Columbia University, Ohio State University, Ohio University, and the University of Michigan.

Some of the data presented in this paper were obtained from the Mikulski Archive for Space Telescopes (MAST) at the STScI. The specific observations analyzed can be accessed via https://doi.org/10.17909/ew79-we39. STScI is operated by the Association of Universities for Research in Astronomy, Inc., under NASA contract NAS5-26555. Support to MAST for these data is provided by the NASA Office of Space Science via grant NAG5-7584 and by other grants and contracts.

This paper includes data collected with the TESS mission, obtained from the MAST data archive at STScI. Funding for the TESS mission is provided by the NASA Explorer Program. STScI is operated by the Association of Universities for Research in Astronomy, Inc., under NASA contract NAS5–26555.

Based on observations obtained with the Samuel Oschin 48-inch Telescope at the Palomar Observatory as part of the Zwicky Transient Facility (ZTF) project. ZTF is supported by the National Science Foundation under Grant No. AST-1440341 and a collaboration including Caltech, IPAC, the Weizmann Institute for Science, the Oskar Klein Center at Stockholm University, the University of Maryland, the University of Washington, Deutsches Elektronen-Synchrotron and Humboldt University, Los Alamos National Laboratories, the TANGO Consortium of Taiwan, the University of Wisconsin at Milwaukee, and Lawrence Berkeley National Laboratories. Operations are conducted by COO, IPAC, and UW.

This publication makes use of data products from the Two Micron All Sky Survey (2MASS), which is a joint project of the University of Massachusetts and the Infrared Processing and Analysis Center/California Institute of Technology, funded by the National Aeronautics and Space Administration and the National Science Foundation.

This publication makes use of data products from the Wide-field Infrared Survey Explorer (WISE), which is a joint project of the University of California, Los Angeles, and the Jet Propulsion Laboratory/California Institute of Technology, and NEOWISE, which is a project of the Jet Propulsion Laboratory/California Institute of Technology. WISE and NEOWISE are funded by the National Aeronautics and Space Administration.

The authors acknowledge the High Performance Computing Center[14] (HPCC) at Texas Tech University for providing computational resources that have contributed to the research results reported within this paper.

This work made use of Astropy:[15] a community-developed core Python package and an ecosystem of tools and resources for astronomy (Astropy Collaboration et al. 2013, 2018, 2022).

Appendix

Here we present the data tables related to the analysis presented in this work. Table A1 contains the radial velocity measurements obtained for each of the 28 new binaries which were used to create Table 2. Table A2 contains the atmospheric parameters for the 287 other objects observed as part of our observation campaign, represented as green points in Figures 1 and 2.

[14] http://www.hpcc.ttu.edu
[15] http://www.astropy.org

Table A1
Radial Velocity Measurements for the 28 New Binaries Identified in This Work

Object	HJD (−2,450,000 days)	v_r (km s^{-1})
J0135+2359	9192.787768	133.7 ± 7.0
J0135+2359	9548.737532	7.4 ± 10.6
J0135+2359	9548.786808	−17.7 ± 10.0
J0135+2359	9548.834528	−72.6 ± 9.5
J0135+2359	9549.572076	110.4 ± 16.5
J0135+2359	9549.712261	117.2 ± 13.1
J0135+2359	9549.776407	139.2 ± 9.6
J0135+2359	9549.821702	74.6 ± 12.7
J0135+2359	9549.827105	98.2 ± 13.5
J0135+2359	9549.831960	84.5 ± 14.8
J0135+2359	9549.837437	103.3 ± 14.2
J0135+2359	9550.562962	−14.0 ± 8.6
J0135+2359	9550.782942	113.2 ± 8.5
J0135+2359	9551.560708	−192.1 ± 10.9
J0135+2359	9551.568185	−200.6 ± 13.3
J0135+2359	9551.574674	−171.2 ± 8.7
J0135+2359	9551.664734	−107.1 ± 8.3
J0135+2359	9551.767718	−1.4 ± 9.1
J0155−4148	8778.528269	120.9 ± 4.5
J0155−4148	8778.747847	93.1 ± 5.5
J0155−4148	8780.584034	107.9 ± 9.8
J0155−4148	8780.591087	62.2 ± 8.2
J0155−4148	8781.538707	199.1 ± 2.5
J0155−4148	8781.631074	103.9 ± 2.0
…	…	…

Note. This table has been truncated. The complete version of this table is available in the supplemental data files.

(This table is available in its entirety in machine-readable form.)

Table A2
Atmospheric Parameters (Assuming Pure-hydrogen Atmospheres) for Objects Observed as Part of Our Follow-up Campaign with $\log g > 5.0$

SOURCE_ID (Gaia DR3)	R.A. (2016.0)	Decl. (2016.0)	$T_{\rm eff}$ (K)	$\log g$ (cm s^{-2})	Gaia G (mag)	Gaia (BP − RP) (mag)	Gaia Parallax (mas)
2882002220454588672	00:03:06.730	+40:39:27.119	19,250 ± 470	8.00 ± 0.07	18.49	0.01 ± 0.01	1.71 ± 0.32
2739093475807603584	00:03:19.659	+02:26:23.089	21,790 ± 1190	8.35 ± 0.18	16.39	−0.098 ± 0.005	6.32 ± 0.07
2798386113507604992[c]	00:03:33.944	+20:16:26.238	17,760 ± 540	7.72 ± 0.10	18.95	0.07 ± 0.02	2.25 ± 0.25
2874194833198918400	00:03:42.161	+32:44:15.731	16,410 ± 440	7.79 ± 0.08	18.22	0.22 ± 0.01	3.30 ± 0.14
2448821478361661696	00:05:04.760	−01:27:08.384	31,340 ± 1380	7.68 ± 0.31	16.63	−0.33 ± 0.01	3.66 ± 0.07
420251387300980096[c]	00:07:09.001	+53:49:47.474	32,980 ± 1930	6.15 ± 0.35	16.17	0.071 ± 0.004	0.96 ± 0.04
2859826106009305216[c]	00:12:32.540	+27:47:09.460	25,990 ± 860	7.37 ± 0.13	16.98	−0.31 ± 0.01	2.89 ± 0.09
2768409887481718272[c]	00:12:45.662	+14:39:56.678	14,580 ± 410	7.38 ± 0.08	18.19	0.07 ± 0.01	2.78 ± 0.18
2800210546895703680[c]	00:15:48.404	+21:27:46.332	32,970 ± 1020	7.35 ± 0.21	17.51	−0.30 ± 0.01	1.85 ± 0.10
2876543282660374784	00:17:44.512	+35:58:26.087	18,410 ± 430	7.95 ± 0.07	18.85	0.03 ± 0.02	1.88 ± 0.23
2863621134816230528[a] [c]	00:18:11.384	+33:11:08.826	30,630 ± 590	7.44 ± 0.09	18.04	−0.29 ± 0.01	1.28 ± 0.14
2855799415254881408	00:20:22.382	+26:40:10.956	11,820 ± 220	8.02 ± 0.13	16.11	−0.111 ± 0.005	10.51 ± 0.05
3805609416774247 68[b]	00:33:52.632	+38:55:29.608	34,130 ± 700	7.30 ± 0.13	18.34	−0.19 ± 0.02	1.19 ± 0.17
4907063048361514496	00:40:00.768	−58:40:31.721	38,240 ± 750	7.28 ± 0.09	17.58	−0.24 ± 0.02	1.14 ± 0.08
2542961560852591744	00:40:22.906	−00:21:30.172	16,470 ± 510	8.16 ± 0.09	14.85	0.046 ± 0.004	18.24 ± 0.03
2550740120286280576	00:45:36.928	+02:40:14.491	15,140 ± 480	5.03 ± 0.10	18.85	0.31 ± 0.02	0.93 ± 0.27
2809085018776598528[c]	00:49:11.206	+28:16:02.255	27,850 ± 2870	5.68 ± 0.42	16.56	−0.32 ± 0.01	0.59 ± 0.07
377520826387065856	00:52:04.391	+45:05:33.799	11,730 ± 180	8.21 ± 0.11	16.01	−0.039 ± 0.004	13.28 ± 0.04
2776836514532338304[c]	00:52:44.411	+13:16:35.972	36,500 ± 1560	7.33 ± 0.28	17.94	−0.32 ± 0.01	1.11 ± 0.13
3744479963289847 04[c]	01:01:10.344	+41:06:04.921	21,740 ± 510	7.36 ± 0.07	18.41	−0.24 ± 0.02	1.68 ± 0.17
2785461702216001152	01:07:25.996	+19:09:32.166	21,940 ± 1260	7.56 ± 0.19	15.64	−0.276 ± 0.005	5.93 ± 0.05
2579742694406440064[c]	01:09:29.505	+09:19:51.845	32,350 ± 1030	7.81 ± 0.23	17.37	−0.36 ± 0.01	1.53 ± 0.11
2534408386884529920	01:12:58.398	−00:59:52.519	19,380 ± 610	7.58 ± 0.10	18.84	−0.27 ± 0.03	1.09 ± 0.25
373358998783703808	01:16:00.832	+42:49:38.323	12,970 ± 200	5.06 ± 0.05	18.71	−0.00 ± 0.02	0.57 ± 0.18
…	…	…	…	…	…	…	…

Notes. Objects which show periodic photometric variability in ZTF DR16 or TESS high-cadence data, and objects which were classified as ELM white dwarf candidates in Pelisoli & Vos (2019), are marked. Optical spectroscopy for each object presented in this table is available in a public Zenodo archive (Kosakowski et al. 2023). This table has been truncated.

[a] Photometric variability: TESS high cadence.

[b] Photometric variability: ZTF.

[c] Pelisoli & Vos (2019) ELM white dwarf candidate.

(This table is available in its entirety in machine-readable form.)

ORCID iDs

Alekzander Kosakowski https://orcid.org/0000-0002-9878-1647
Warren R. Brown https://orcid.org/0000-0002-4462-2341
Mukremin Kilic https://orcid.org/0000-0001-6098-2235
Thomas Kupfer https://orcid.org/0000-0002-6540-1484
Antoine Bédard https://orcid.org/0000-0002-2384-1326
A. Gianninas https://orcid.org/0000-0002-8655-4308
Marcel A. Agüeros https://orcid.org/0000-0001-7077-3664
Manuel Barrientos https://orcid.org/0000-0002-6153-9304

References

Althaus, L. G., Miller Bertolami, M. M., & Córsico, A. H. 2013, A&A, 557, A19
Abazajian, K., Adelman-McCarthy, J. K., Agüeros, M. A., et al. 2003, AJ, 126, 2081
Amaro-Seoane, P., Andrews, J., Arca Sedda, M., et al. 2023, LRR, 26, 2
Amaro-Seoane, P., Audley, H., Babak, S., et al. 2017, arXiv:1702.00786
Astropy Collaboration, Price-Whelan, A. M., Lim, P. L., et al. 2022, ApJ, 935, 167
Astropy Collaboration, Price-Whelan, A. M., Sipőcz, B. M., et al. 2018, AJ, 156, 123
Astropy Collaboration, Robitaille, T. P., Tollerud, E. J., et al. 2013, A&A, 558, A33
Bédard, A., Bergeron, P., Brassard, P., et al. 2020, ApJ, 901, 93
Bédard, A., Bergeron, P., & Fontaine, G. 2017, ApJ, 848, 11
Bellm, E. C., Kulkarni, S. R., Graham, M. J., et al. 2019, PASP, 131, 018002
Bloemen, S., Groot, P., Nelemans, G., et al. 2015, in ASP Conf. Ser. 496, (Living Together: Planets, Host Stars and Binaries) ed. S. M. Rucinski, G. Torres, & M. Zejda (San Francisco, CA: ASP), 254
Bours, M. C. P., Marsh, T. R., Parsons, S. G., et al. 2014, MNRAS, 438, 3399
Brown, W. R., Gianninas, A., Kilic, M., et al. 2016a, ApJ, 818, 155
Brown, W. R., Kilic, M., Kenyon, S. J., et al. 2016b, ApJ, 824, 46
Brown, W. R., Kilic, M., Allende Prieto, C., et al. 2010, ApJ, 723, 1072
Brown, W. R., Kilic, M., Allende Prieto, C., et al. 2012, ApJ, 744, 142
Brown, W. R., Kilic, M., Allende Prieto, C., et al. 2013, ApJ, 769, 66
Brown, W. R., Kilic, M., Kosakowski, A., et al. 2020, ApJ, 889, 49
Brown, W. R., Kilic, M., Kosakowski, A., et al. 2022, ApJ, 933, 94
Burdge, K. B., Coughlin, M. W., Fuller, J., et al. 2019, Natur, 571, 528
Burdge, K. B., Prince, T. A., Fuller, J., et al. 2020, ApJ, 905, 32
Chambers, K. C., Magnier, E. A., Metcalfe, N., et al. 2016, arXiv:1612.05560
Chiba, M., & Beers, T. C. 2000, AJ, 119, 2843
Claret, A., Cukanovaite, E., Burdge, K., et al. 2020, A&A, 634, A93
Clemens, J. C., Crain, J. A., & Anderson, R. 2004, Proc. SPIE, 5492, 331
Copperwheat, C. M., Marsh, T. R., Dhillon, V. S., et al. 2010, MNRAS, 402, 1824
Coughlin, M. W., Burdge, K., Phinney, E. S., et al. 2020, MNRAS Lett., 494, L91
Finch, E., Bartolucci, G., Chucherko, D., et al. 2023, MNRAS, 522, 5358
Gianninas, A., Bergeron, P., & Ruiz, M. T. 2011, ApJ, 743, 138
Gianninas, A., Dufour, P., Kilic, M., et al. 2014, ApJ, 794, 35
Gianninas, A., Kilic, M., Brown, W. R., et al. 2015, ApJ, 812, 167
Graham, M. J., Kulkarni, S. R., Bellm, E. C., et al. 2019, PASP, 131, 078001
Gaia Collaboration, Brown, A. G. A., Vallenari, A., et al. 2018, A&A, 616, A1
Gaia Collaboration, Brown, A. G. A., Vallenari, A., et al. 2021, A&A, 649, A1
Gaia Collaboration, Vallenari, A., Brown, A. G. A., et al. 2022, arXiv:2208.00211
Heber, U. 2023, arXiv:2304.02969
Hermes, J. J., Brown, W. R., Kilic, M., et al. 2014, ApJ, 792, 39
Irrgang, A., Geier, S., Heber, U., et al. 2021, A&A, 650, A102

Irrgang, A., Przybilla, N., & Meynet, G. 2022, NatAs, 6, 1414
Istrate, A. G., Marchant, P., Tauris, T. M., et al. 2016, A&A, 595, A35
Ivezić, Ž., Kahn, S. M., Tyson, J. A., et al. 2019, ApJ, 873, 111
Kenyon, S. J., & Garcia, M. R. 1986, AJ, 91, 125
Kilic, M., Bédard, A., Bergeron, P., et al. 2020, MNRAS, 493, 2805
Kilic, M., Brown, W. R., Allende Prieto, C., et al. 2011, ApJ, 727, 3
Kilic, M., Brown, W. R., Allende Prieto, C., et al. 2012, ApJ, 751, 141
Kilic, M., Brown, W. R., Heinke, C. O., et al. 2016, MNRAS, 460, 4176
Kilic, M., Moss, A. G., Kosakowski, A., et al. 2023, MNRAS, 518, 2341
Kilic, M., Stanek, K. Z., & Pinsonneault, M. H. 2007, ApJ, 671, 761
Korol, V., Rossi, E. M., Groot, P. J., et al. 2017, MNRAS, 470, 1894
Kosakowski, A., Brown, W., Kilic, M., et al. 2023, The ELM Survey South II [Data set], Zenodo, doi:10.5281/zenodo.7849976
Kosakowski, A., Kilic, M., Brown, W. R., et al. 2020, ApJ, 894, 53
Kovács, G., Zucker, S., & Mazeh, T. 2002, A&A, 391, 369
Kupfer, T., Korol, V., Littenberg, T. B., et al. 2023, arXiv:2302.12719
Kupfer, T., Prince, T. A., van Roestel, J., et al. 2021, MNRAS, 505, 1254
Kurtz, M. J., & Mink, D. J. 1998, PASP, 110, 934
Li, Z., Chen, X., Chen, H.-L., et al. 2019, ApJ, 871, 148
Li, Z., Chen, X., Chen, H.-L., et al. 2020, ApJ, 893, 2
Liebert, J., Bergeron, P., & Holberg, J. B. 2005, ApJS, 156, 47
Lomb, N. R. 1976, Ap&SS, 39, 447
Mainzer, A., Bauer, J., Grav, T., et al. 2011, ApJ, 731, 53
Martin, D. C., Fanson, J., Schiminovich, D., et al. 2005, ApJL, 619, L1
Masci, F. J., Laher, R. R., Rusholme, B., et al. 2019, PASP, 131, 018003
Nelemans, G., Yungelson, L. R., & Portegies Zwart, S. F. 2001, A&A, 375, 890
Onken, C. A., Wolf, C., Bessell, M. S., et al. 2019, PASA, 36, e033
Pelisoli, I., & Vos, J. 2019, MNRAS, 488, 2892
Przybilla, N., Nieva, M.-F., & Butler, K. 2011, JPhCS, 328, 012015
Ricker, G. R., Winn, J. N., Vanderspek, R., et al. 2015, JATIS, 1, 014003
Roelofs, G. H. A., Groot, P. J., Benedict, G. F., et al. 2007, ApJ, 666, 1174
Scargle, J. D. 1982, ApJ, 263, 835
Scherbak, P., & Fuller, J. 2023, MNRAS, 518, 3966
Schlafly, E. F., & Finkbeiner, D. P. 2011, ApJ, 737, 103
Schönrich, R., Binney, J., & Dehnen, W. 2010, MNRAS, 403, 1829
Shanks, T., Metcalfe, N., Chehade, B., et al. 2015, MNRAS, 451, 4238
Shen, K. J. 2015, ApJL, 805, L6
Skrutskie, M. F., Cutri, R. M., Stiening, R., et al. 2006, AJ, 131, 1163
Southworth, J. 2013, A&A, 557, A119
Southworth, J., Maxted, P. F. L., & Smalley, B. 2004, MNRAS, 351, 1277
Stassun, K. G., Oelkers, R. J., Pepper, J., et al. 2018, AJ, 156, 102
Timpano, S. E., Rubbo, L. J., & Cornish, N. J. 2006, PhRvD, 73, 122001
Tremblay, P.-E., Gianninas, A., Kilic, M., et al. 2015, ApJ, 809, 148
Tremblay, P.-E., Ludwig, H.-G., Steffen, M., et al. 2011, A&A, 531, L19
VanderPlas, J. T. 2018, ApJS, 236, 16
Wang, K., Németh, P., Luo, Y., et al. 2022, ApJ, 936, 5
Wright, E. L., Eisenhardt, P. R. M., Mainzer, A. K., et al. 2010, AJ, 140, 1868
Zhang, X., Jeffery, C. S., Chen, X., et al. 2014, MNRAS, 445, 660